Impedance Measurement and Estimation of Three-Phase Voltage-Source Converters

Gong, Hong

DOI (link to publication from Publisher):
10.5278/vbn.phd.eng.00085

Publication date:
2020

Document Version
Publisher's PDF, also known as Version of record

IMPEDANCE MEASUREMENT AND ESTIMATION OF THREE-PHASE VOLTAGE-SOURCE CONVERTERS

BY
HONG GONG

DISSERTATION SUBMITTED 2020

AALBORG UNIVERSITY
DENMARK

Impedance Measurement and Estimation of Three-Phase Voltage-Source Converters

by

Hong Gong

Department of Energy Technology

Aalborg University, Denmark

AALBORG UNIVERSITY
DENMARK

Dissertation submitted December, 2020.

Dissertation submitted: December, 2020

PhD supervisor: Prof. Xiongfei Wang,
Aalborg University

PhD committee: Associate Professor Daniel Ioan Stroe (chairman)
Aalborg University

Professor Xavier Guillaud
Ecole Centrale de Lille

Team Leader for Power Electronics Nan Chen
Hitachi ABB Power Grids Research

PhD Series: Faculty of Engineering and Science, Aalborg University

Department: Department of Energy Technology

ISSN (online): 2446-1636
ISBN (online): 978-87-7210-864-3

Published by:
Aalborg University Press
Kroghstræde 3
DK – 9220 Aalborg Ø
Phone: +45 99407140
aauf@forlag.aau.dk
forlag.aau.dk

Printed in Denmark by Rosendahls, 2021

English Summary

Voltage-source converters (VSCs) have been extensively used with the integration of renewable energy resources into power grids. Due to mutual interactions between control dynamics of VSCs and power grids, oscillations are prone to occur in a wide frequency range. In order to analyze and mitigate the oscillations, the impedance-based modeling and stability analysis methods have been increasingly applied to VSC-based power systems. However, it is hard for system operators to get the analytical impedance model since they cannot access the internal control systems of VSCs from different vendors. Therefore, there is an important need to directly measure and/or estimate the impedance profile from the terminals of VSCs.

The impedance model of three-phase VSCs is commonly measured in the *dq*-frame that is aligned with the voltage vector at the terminal of VSC, since time-invariant dc operating points of VSCs can be obtained through the *dq*-transformation of ac operating trajectories. The *dq*-frame impedance measurement technique has been continuously evolving in recent years. Several research problems that can influence the accuracy and efficiency of impedance measurement have been identified, which include the perturbation signal design, the impact of *dq*-transformation, and the impedance calculation method.

This Ph.D. thesis presents a comprehensive investigation into the identified research problems, and develops a series of solutions to improve the accuracy and efficiency of *dq*-frame impedance measurement. First, a systematic design method of perturbation signal is proposed, where a set of performance indices is defined to guide the selection of perturbation signal type, and then the frequency components of the selected perturbation signal are intentionally designed to avoid the frequency-overlapping issue caused by nonlinear dynamics of VSCs control. Second, the impact of *dq*-transformation is analyzed by considering the dynamics of the used phase angle, which are caused by 1) the dynamic effect of the used phase-locked loop (PLL), and 2) the variation of fundamental frequency in future low inertia grids. An improved PLL is then proposed to improve the accuracy of *dq*-frame impedance measurement. Lastly, the coupling effect of grid impedance on the traditional multiple-input multiple-output (MIMO) impedance calculation is analyzed, and a time-domain MIMO parametric identification method is further developed to mitigate such effect.

While the *dq*-frame impedance of three-phase VSCs can be accurately measured with the proposed methods, it is only valid for a given operating point. This is due to the fact that the impedance measurement is, in essence, a linearization process of VSCs around an equilibrium point. Consequently, the measured VSC impedance can only be used to predict the system stability at a single operating point. To address this challenge, this Ph.D. project explores linear interpolation techniques and develops an approach to estimating the *dq*-frame impedance of three-phase VSCs in a wide range

of operating points, yet with a limited set of measurement data. Further, a criterion for determining the needed set of measurement data is developed based on the posterior error estimation method.

It is concluded at the end of this thesis that the accuracy and efficiency of the *dq*-frame impedance measurement are improved with the proposed methods. An impedance estimation technique is also developed to predict the *dq*-frame impedance model at a wide range of operating points.

Dansk Resume

Spændingskildeomformere (VSC'er) er blevet brugt i vid udstrækning med integrationen af vedvarende energikilder i strømnettet. På grund af gensidige interaktioner mellem styringsdynamik af VSC'er og elnet er svingninger tilbøjelige til at forekomme i et bredt frekvensområde. For at analysere og afbøde svingningerne er de impedansbaserede modellerings- og stabilitetsanalysemetoder i stigende grad blevet anvendt på VSC-baserede elsystemer. Det er imidlertid svært for systemoperatører at få den analytiske impedansmodel, da de ikke kan få adgang til VSCs interne kontrolsystemer fra forskellige leverandører. Derfor er der et vigtigt behov for direkte at måle og / eller estimere impedansprofilen fra terminalerne på VSC'er.

Impedansmodellen for trefasede VSC'er måles almindeligvis i dq-rammen, der er justeret med spændingsvektoren ved terminalen på VSC, da tidsinvarante DC-driftspunkter for VSC'er kan opnås gennem dq-transformation af vekselstrømsoperationsbaner . Dq-frame impedansmålingsteknikken har udviklet sig kontinuerligt i de senere år. Flere forskningsproblemer, der kan påvirke nøjagtigheden og effektiviteten af impedansmåling, er blevet identificeret, som inkluderer forstyrrelsessignaldesignet, virkningen af dq-transformation og impedansberegningsmetoden.

Denne ph.d. afhandlingen præsenterer en omfattende undersøgelse af de identificerede forskningsproblemer og udvikler en række løsninger til at forbedre nøjagtigheden og effektiviteten af dq-frame impedansmåling. For det første foreslås en systematisk designmetode for forstyrrelsessignal, hvor et sæt ydeevneindekser er defineret til at styre valget af forstyrrelsessignaltype, og derefter er frekvenskomponenterne i det valgte forstyrrelsessignal bevidst designet til at undgå det forårsagede frekvensoverlappende problem ved hjælp af ikke-lineær kontroldynamik af VSC'er. For det andet analyseres virkningen af dq-transformation ved at overveje dynamikken i den anvendte fasevinkel, som er forårsaget af 1) den dynamiske effekt af den anvendte faselåste sløjfe (PLL) og 2) variationen af grundlæggende frekvens i fremtiden lave inerti gitre. En forbedret PLL foreslås derefter for at forbedre nøjagtigheden af dq-frame impedansmåling. Endelig analyseres koblingseffekten af gitterimpedans på den traditionelle multiple-input multiple-output (MIMO) impedansberegning, og en tidsdomæne MIMO parametrisk identifikationsmetode udvikles yderligere for at afbøde en sådan effekt.

Mens dq-rammeimpedansen for trefasede VSC'er kan måles nøjagtigt med de foreslåede metoder, er den kun gyldig for et givet driftspunkt. Dette skyldes det faktum, at impedansmålingen i det væsentlige er en lineariseringsproces af VSC'er omkring et ligevægtspunkt. Derfor kan den målte VSC-impedans kun bruges til at forudsige systemstabiliteten på et enkelt driftspunkt. For at tackle denne udfordring

er denne ph.d. projektet udforsker interpolationsteknikker og udvikler en tilgang til estimering af dq-frame impedans af trefasede VSC'er i en lang række driftspunkter, dog med et begrænset sæt måledata. Yderligere udvikles et kriterium til bestemmelse af det nødvendige sæt måledata baseret på den bageste fejlestimeringsmetode.

Det konkluderes i slutningen af denne afhandling, at nøjagtigheden og effektiviteten af dq-frame impedansmåling forbedres med de foreslåede metoder. En impedansestimeringsteknik er også udviklet til at forudsige impedansmodellen ved en lang række driftspunkter.

Acknowledgments

This Ph.D. project is funded by the China Scholarship Council (CSC) and the Department of Energy Technology, Aalborg University, Denmark. I would like to express my acknowledgment of these supports.

First and foremost, I would like to express my sincere gratitude to my supervisor, Prof. Xiongfei Wang, for his insightful guidance and constant patience in all academic aspects during the three years. Without his help and encouragement, I cannot come this far from my humble beginning. I am also grateful for the opportunity he provided to work with the great engineers in Hitachi ABB, especially Lennart, Jean-Philippe, Christer, and Hongyang. The four-month experience in Västerås will keep reminding me to keep my work down-to-earth in my future career.

Then, my special thanks go to Dr. Dongsheng Yang, for his guidance and constant encouragement from the very beginning of my Ph.D. study. His kind support is the silver lining when the day is gloomy.

Also, I would like to thank all the excellent people I meet in Aalborg. I appreciate all the collaboration and discussion in the eGrid research program, especially Heng and Yicheng. And I really enjoy all the dinner parties and sports games, which attribute to my friends: Bing, Bo, Chao, Dapeng, Donghua, Fangzhou, Haoran, He, Jinkui, Jiahui, Jing, Joachim, Mads, Meng, Mengfan, Peng, Qiao, Shihfeng, Teng, Wei, Xiaoling, Xiaolong, Yi, Yinzhou, Zhongxu, Zhongting, Zhengge, and Zhan. I also thank all the kind support from the staff at the Department of Energy Technology, Aalborg University.

Finally, I want to thank my family, especially my wife Wenting, for their unconditional love and support.

Hong Gong

Aalborg University, December, 2020

Table of Contents

Table of Figures

Table of Tables

Chapter 1. Introduction

1.1. Background and Challenges

Voltage-source converters (VSCs) have been extensively applied in the power system, including renewable energy-based power generation systems [1], high-voltage dc transmission (HVDC) systems [2], and flexible AC transmission systems (FACTS) [3]. With the proliferation of VSCs in the power system, growing dynamic issues have been occurred in a wide frequency range due to the mutual interactions between wide-time scale control loops of VSCs and with the power grid [4]-[6].

To address these challenges, the impedance-based approach has been increasingly utilized to evaluate the stability of the VSC-based system [7]-[10]. Nevertheless, the analytical impedance model of VSC is hard to obtain in practice, since power system operators do not get access to the internal control systems of VSCs due to the confidentiality of VSC-based equipment manufacturers. Thus, there is an increasing demand for measuring and estimating the impedance profile directly from the "black-box" models of VSCs.

Three-phase VSCs are, in general, nonlinear and time-varying dynamical systems, where the nonlinearity is due to the outer power control and synchronization control, and the time variance results from the time-periodic operating trajectories of the ac system [11]. Therefore, the impedance model of three-phase VSCs is commonly measured in the synchronous reference (*dq*) frame that is aligned with the voltage vector at the terminal of VSC [12]-[14], since the time-invariant dc operating points can be yielded from the time-varying ac operating trajectories through the Park transformation.

Fig. 1.1 depicts the simplified one-line diagram of the three-phase VSC, where $\boldsymbol{Z}_{\mathbf{dq}}$ denotes the impedance matrix of the VSC in the *dq*-frame, which can be extracted at the Point of Connection (PoC) of the VSC-connected system. The *dq*-frame impedance matrix of three-phase VSC are calculated based on current and voltage responses at the *d*- and *q*-axes, which is expressed as

$$\begin{bmatrix} \Delta U_d \\ \Delta U_q \end{bmatrix} = \mathbf{Z}_{dq} \begin{bmatrix} \Delta I_d \\ \Delta I_q \end{bmatrix} = \begin{bmatrix} Z_{dd} & Z_{dq} \\ Z_{qd} & Z_{qq} \end{bmatrix} \begin{bmatrix} \Delta I_d \\ \Delta I_q \end{bmatrix} \tag{1.1}$$

where △ represents the small-signal variations from the equilibrium point of *dq*-axis voltage and current.

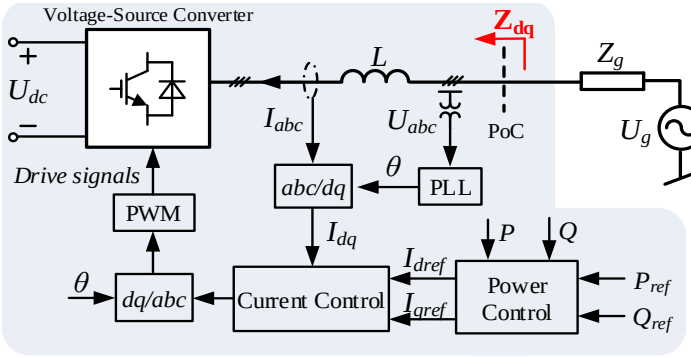

Fig. 1.1. Simplified one-line diagram of the three-phase VSC.

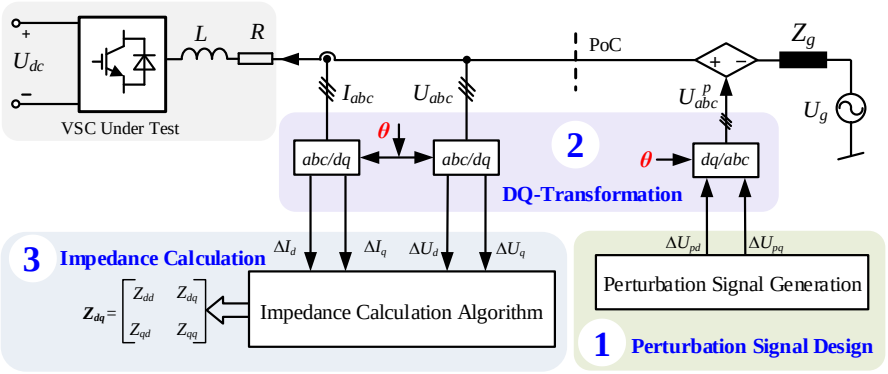

Figure 1.2. Block diagram of the *dq*-frame impedance measurement of three-phase VSC.

The basic idea of impedance measurement is to acquire the voltage and current responses at the frequency of interest from the terminal of measured VSC, and then extract the frequency-dependent impedance of VSCs. Fig. 1.2 illustrates the block diagram of the *dq*-frame impedance measurement of three-phase VSC, which consists of three parts: 1) the perturbation signal design, 2) *dq*-transformations, and 3) the impedance calculation based on the voltage and current responses. Each part may challenge the accuracy and/or efficiency of the impedance measurement.

To measure the impedance model of VSC at the frequency of interest, the acquired voltage and current responses should contain the frequency components of interest. Yet, during the normal operation of the VSC-based system, the measured responses cannot cover the whole frequency range. Therefore, perturbation signals are needed to excite the VSC-based system at desired frequencies so that the impedance model can be calculated from the measured responses.

Once the VSC is perturbed with designed signals, the voltage and current responses of VSC are measured. Since the impedance is measured in the *dq*-frame, the acquired voltage and current need to be transformed from the *abc* frame to the *dq* frame through the *dq*-transformation. However, the phase angle used with the *dq*-transformation may involve additional dynamics, which may bring errors in the transformed voltages and currents in the *dq* frame, and consequently affect the accuracy of impedance measurement.

Based on the transformed *dq*-frame voltage and current, the entries of the *dq*-frame impedance matrix of VSC can be calculated. Yet, to obtain the four entries of the *dq*-frame impedance matrix, two measurement cycles are usually required [15], which is inefficient and the calculation accuracy can be affected by the variation of the operating point. Further, this method ignores the coupling effect of the external grid impedance, which can lead to inaccurate impedance measurement. . Therefore, the impedance calculation method may affect both the accuracy and efficiency of the impedance measurement.

Lastly, even though the *dq*-frame impedance of three-phase VSCs can be accurately measured, it is only effective at the specific operating point, since the *dq*-frame impedance measurement is essentially a linearization process of three-phase VSC around the equilibrium operating point. However, the operating points of VSCs may vary with the grid conditions. Thus, the impedance model of VSC changes and the measured impedance at a specific operating point can be inadequate for the stability analysis of VSC-based power systems.

1.2. State of the Art

To improve the accuracy and efficiency of the *dq*-frame impedance measurement for VSCs, a number of research efforts have been made on each part of the impedance measurement and on impedance estimation. The state-of-the-art for each part is reviewed.

1.2.1. Perturbation Signal Design

From the perspective of the perturbation signal design, the impedance measurement can be invasive and non-invasive. The non-invasive method does not need extra equipment and intentional perturbation injection, and it merely utilizes the natural voltage and current variations caused by the event or disturbance [16], [17]. However, the harmonic content of the perturbations generated from the event, such as transformer energization and fault cannot be controlled [18]. In addition, the event cannot be performed anytime and usually cannot be repeated, which challenges the efficiency of the impedance measurement [19]. As for the perturbations generated by the disturbance, for instance, the existed harmonics originated from the line-

commutated converter (LCC)-HVDC [20], the measurement can be conducted anytime and it does not disturb the normal operation of the system. Yet, the harmonic content of the disturbance is limited and it is also sensitive to background harmonics, which may not be able to yield the accurate impedance model at all frequency range of interest [21]

On the contrary, the invasive method usually gives more accurate results due to the intentional injection of a significant level of perturbation, which allows achieving a higher signal to noise ratio (SNR). However, the perturbation signal should be intentionally designed before it is injected into the system so that the system responses can be sufficiently excited. There are many types of perturbation signals that can be used for the impedance measurement and different signals can have different effects on the accuracy of measurement results. In terms of the power spectrum, the perturbation signals can be classified as the single-frequency perturbation signal and the wideband perturbation signal [22], as illustrated in Fig .1.3 and Fig. 1.4, respectively. Regarding the single-frequency perturbation signal, such as the sinusoidal signal [23], it is injected into the system at one frequency point and the impedance is then measured at the corresponding frequency [24]. Since the total

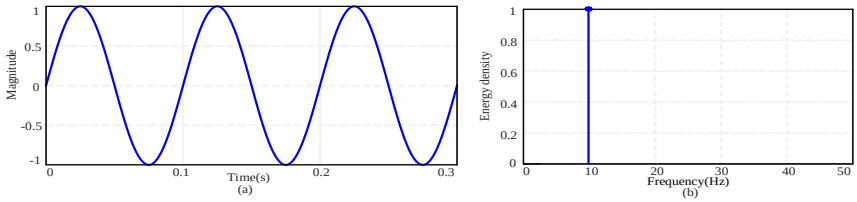

Fig. 1.3. Example of single-frequency perturbation signal (10 Hz sinusoidal signal). (a) Time-domain waveform. (b) Power spectrum.

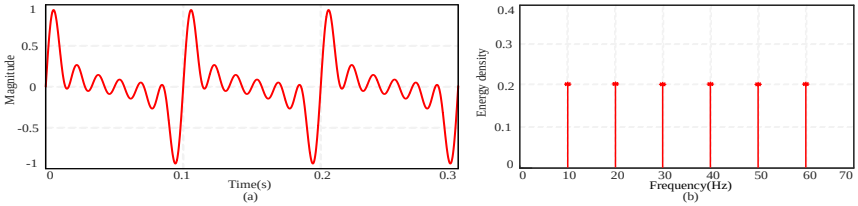

Fig. 1.4. Example of wideband perturbation signal (multi-sinusoidal signal). (a) Time-domain waveform. (b) Power spectrum.

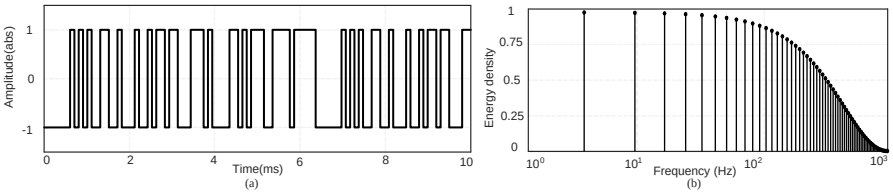

Fig. 1.5. Example of the PRBS signal. (a) Time-domain waveform. (b) Power spectrum

energy of the injected signal is only located at a single frequency point, the signal can achieve a high SNR and consequently improves the measurement accuracy. However, numerous measurements need to be implemented to obtain the wideband characteristics of the impedance model, which is time-consuming and inefficient.

It is thus more efficient to inject wideband perturbation signals that can obtain the impedance characteristic with a single measurement [25]-[29], which can lower the measurement effort and enhance the efficiency of the impedance measurement. Different kinds of wideband perturbation signals have been implemented for the impedance measurement, such as the impulse signal [25], step signal [26], multi-sinusoidal signal [27], pseudo-random binary sequence (PRBS) signal [28], and discrete-interval binary sequence (DIBS) signal [29]. Impulse signal has a white spectrum and can perturb the system at the same level for all the frequencies [25]. However, the high peak value of the impulse signal injected into the system may cause serious nonlinear responses from the measured VSCs. Step signals have also been used for the measurement in [26]. The signal is easy to generate yet it changes the operating point of the measured VSCs and might change the linearization results for the impedance measurement. The multi-sinusoidal perturbation signal is the sum of multiple harmonic signals, which have the same energy density at each harmonic frequency [27]. Yet, the peak value of the summed signals increases when more injected frequencies are desired, which might drive the measured VSCs way out of its linear operating range. To avoid the possible nonlinear responses caused by the high peak value of the impulse signal and multi-sinusoidal signal, the PRBS is adopted in [28]. It is set to fit a specific spectrum and is easily generated by using the pseudo-random number generation algorithm [29]. Nevertheless, the energy density of PRBS at the high-frequency range is very small, as shown in Fig. 1.5, which may result in a low SNR and deteriorate the accuracy of the measurement results in the high-frequency range. Thus, a DIBS is recently reported to replace PRBS, and the *dq*-frame impedance model of VSC measured by using two different types of perturbation signals are compared in [30]. While many types of wideband perturbation signals are available, their performances for the *dq*-frame impedance measurement have not been compared. Further, there is no guidance on selecting the type of perturbation signal utilized for the *dq*-frame impedance measurement of VSC.

In addition, the frequency composition of the perturbation signal also affects the accuracy of the impedance measurement results, in the presence of background harmonics and nonlinear distortions. The guidance on the frequency selection of the perturbation signal is developed in [31] to mitigate the background harmonics impacts on $\alpha\beta$-frame impedance measurement results of VSC. A wideband perturbation signal is employed to measure the *dq*-frame impedance model of a three-phase rectifier. For comparison, the sinusoidal signal is utilized to scan the same impedance model [32]. The differences are originated from the frequency-overlapping in responses, where the components located at perturbation frequencies are mixed with the nonlinear sideband harmonics of six-pulse diode rectifiers [33]. Yet, due to the power control,

the three-phase VSC is a nonlinear system. The injection of wideband perturbation signal may also result in the frequency-overlapping in responses, which causes inaccurate measurement results of *dq*-frame impedance model of VSCs. Therefore, the frequency components of the selected perturbation signal need to be carefully designed to suppress the impact.

1.2.2. Impact of DQ-Transformation

After the injection of the perturbation signal into the system, the terminal voltages and currents of three-phase VSC are measured and recorded in the *abc*-frame since neither *d*-axis nor *q*-axis terminal exists in the real systems. To obtain the *dq*-frame impedance model of three-phase VSC, the *dq*-transformation is needed to transform the responses from the *abc*-frame into the *dq*-frame. As a consequence, the phase angle used with the *dq*-transformation is required.

The phase angle is usually estimated through a PLL or other mathematical algorithms. However, due to the injection of the perturbation signal, the synchronization dynamics might be introduced by the phase angle estimation method, whose impacts on the *dq*-frame impedance measurement are scarcely discussed. The phase angle, which is utilized for the impedance measurement is obtained through the synchronization of grid voltage with an oscillator [34]. However, it is difficult to acquire the grid voltage in the practical system. In [35], the Discrete Fourier Transform (DFT) is directly applied to the PCC voltage to extract the phase angle. Yet, large phase errors may be introduced on the synchronization phase angle even if the system has a small fundamental frequency drift during the impedance measurement.

To eliminate the negative effects of the fundamental frequency variation on the estimated phase angle, the system frequency is monitored online by using the PLL, which can track the phase angle of PCC voltage in real-time and use it for the impedance measurement. Consequently, the PLL, which is employed for the synchronization control of VSC is directly utilized to calculate the phase angle for the *dq*-frame impedance measurement of VSC [36]. However, to guarantee the controller performance, the PLL bandwidth inside the converter is comparatively high, which might result in large errors in the estimated phase angle due to the injected perturbations. The inaccurate phase angel further yields the inaccurate measurement results of the *dq*-frame impedance model especially below the PLL bandwidth frequency range [37]. For the mitigation of these errors, an additional PLL whose bandwidth is designed much lower than the lowest frequency of the injected perturbation signal is utilized to calculate the synchronization phase angle for the impedance measurement [38]. Nevertheless, a slow PLL needs a longer time to acquire the precise phase angle used for the impedance measurement, which deteriorates the measurement efficiency. Further, the frequency of the VSC-connected system might vary, and much lower bandwidth of PLL may not be able to track the

frequency variations. As a consequence, an imprecise phase angle is calculated for the *dq*-transformation, which bring about errors in the transformed *dq*-axis voltage and current response and further results in wrong measurement results.

Further, the impact of synchronization dynamics introduced by PLL on the measurement results is investigated and a mitigation approach is then reported in [39]. Yet, the approach does not consider the impact of the variation of system fundamental frequency, and measurement errors may still exist in several frequency points that are below the PLL bandwidth.

1.2.3. Impedance Calculation Method

Fig. 1.6 illustrates the impedance calculation methods for single-input single-output (SISO) linear-time invariant (LTI) systems. Based on the measured current and voltage, the impedance can be calculated by using the nonparametric identification method e.g., DFT [40] or the parametric identification [41] method, which further yields the frequency response model [42] and the transfer function model [43], respectively. The impedance calculation method plays an important role in both the accuracy and efficiency of impedance measurement [44]-[47]. For the *dq*-frame impedance measurement of three-phase VSC, the processed *dq*-frame voltage and current responses are utilized for the impedance calculation. Since the impedance model of three-phase VSCs in the *dq*-frame is a MIMO system, the elements of the impedance matrix are calculated one by one from the voltage and current responses in either *d*- or *q*- axis based on the DFT [44], [45] or parametric identification method [46]. Nevertheless, both calculation methods have not considered the coupled responses contributed from the cross-coupling between the *d*- and *q*-axis of the grid impedance matrix. As a consequence, the accuracy of the *dq*-frame impedance measurement results might be affected [47].

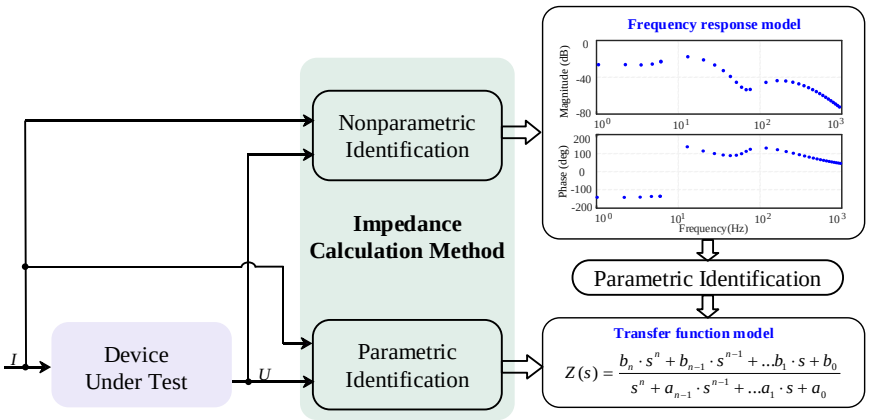

Fig. 1.6. Impedance calculation methods for SISO LTI systems. Source: [42]

To mitigate the impact of the coupling effect on the measurement results, the impedance matrix of VSC is directly calculated based on four established equations, where DFT is applied to the processed voltages and currents in the *dq*-frame after the separate injection of two linearly independent perturbation signals [48]-[50]. The coupling effects of the grid impedance on the calculated impedance results are avoided by identifying the transfer function of the decoupling matrix that maps the transformed relationship between the coupled transfer functions and the uncoupled ones based on the parametric identification method [51]. However, this method needs at least two measurement periods to separately calculate the elements of the impedance matrix of VSC in the *dq*-frame, which is time-consuming and inefficient. Moreover, the operating points of measured VSC may change in renewable power generation systems, which may cause imprecise impedance calculation in case the impedance measurement time is long.

To efficiently measure the *dq*-frame impedance model of VSC, the MIMO impedance calculation method is recently proposed based on the DFT [52]-[55], where two uncorrelated perturbation signals whose power spectrum do not coincide with each other at all perturbation frequencies, are injected on the *d*- and *q*-axes at the same time. Given different frequency compositions of two perturbation signals, the diagonal elements of the VSC impedance matrix are calculated at one time, which improves the efficiency of the impedance measurement. Yet, those works ignore the impact of cross-coupling caused by the grid impedance, which may still cause wrong impedance calculations results [56]. Further, the frequency resolution for DFT needs to be carefully selected to avoid spectrum leakage, since the measured voltage and current responses consist of multiple frequency components [57]. Therefore, there is a need to develop an impedance calculation method that can avoid the impacts of the grid impedance and simultaneously achieve the efficient impedance measurement of VSC.

1.2.4. Impedance Estimation Technique

Even though the impedance model of VSCs can be accurately measured at one operating point, it may not be valid when the operating point changes. To cope with this challenge, a multi-operating-point small-signal modeling method for three-phase VSCs is proposed in [58]-[61]. Given a series of operating points, a set of *dq*-frame impedance models are correspondingly identified based on the time-domain measurement data. The nonlinear weight functions are then multiplied with those identified models, estimating the unmeasured impedance model by means of different weighted sums of the identified models, as shown in Fig. 1.6. This method needs the use of the parametric identification method to identify the transfer functions of impedance models from the time-domain data, which turns to be more complex than the frequency-domain measurements since the model structure and order need to be pre-selected [62], [63].

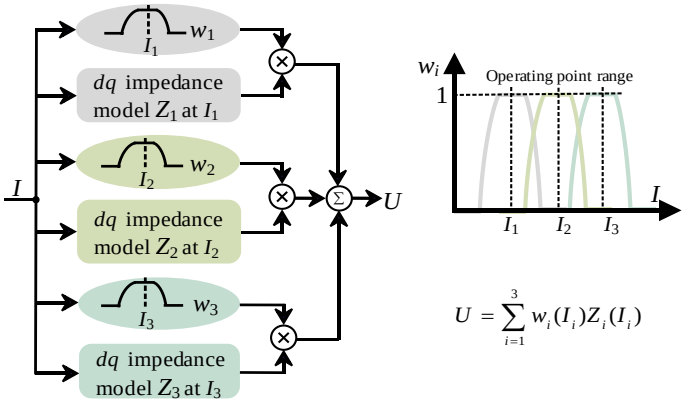

Fig. 1.6. One-dimensional *dq*-frame impedance model of VSC covering multi-operating points. Source: [58].

To avoid using the time-domain parametric identification, a multi-operating-point impedance model that is based on the frequency-domain measurement results is recently reported in [64], where the artificial neural network (ANN) is employed to map the nonlinear relationship between the VSC impedance model and operating points. However, there is a lack of clear guidance for the ANN training process, i.e., the initialization of ANN structure, the selection for the number of hidden layers, and the number of neurons in each layer, which significantly influences the estimation accuracy and is challenging for the practical application. Further, the multi-operating-point impedance model identified from either the time-domain data [58]-[61] or the frequency-domain measurement results [64] requires the utilization of nonlinear weight functions to estimate the unmeasured admittance models through the different weighted combinations of measured admittance models, which makes the approach tedious and complicated. Further, the utilization of nonlinear weight functions makes the approach more cumbersome and complicated.

To avoid using nonlinear weight functions, an impedance model that is approximated to be linearly dependent on operating points is developed [65]. With the prior knowledge of the control structure of the converter, the admittance profile is reformulated as a function of operating points and the controller parameters. Given a set of measurement results at different operating points, a group of homogeneous linear equations is obtained to solve unknown control parameters, such that the admittance model can be calculated as a function of constant control parameters and varying operating variables. Yet, the method is essentially a linear approximation to the nonlinear relationship between the admittance model and operating points, and its accuracy is highly dependent on the number of measured operating points. Hence, how to choose the number of measured operating points still remains a challenge.

1.3. Research Gaps and Main Objectives

1.3.1. Research Gaps

Based on the state-of-the-art, the research gap for the perturbation signal design, the impact of *dq*-transformation, impedance calculation method, and impedance estimation technique can be summarized as follow:

1. Research Gap (RG.1): It is still unclear how to select the perturbation signal type and determine the frequency components of the selected perturbation signal in the presence of nonlinear dynamics.

2. Research Gap (RG.2): It is unclear how the synchronization dynamics introduced by the variation of fundamental frequency affect the accuracy of impedance measurement.

3. Research Gap (RG.3): The coupling effect of the grid impedance on the conventional MIMO impedance calculation method has been overlooked, which might jeopardize the measurement results.

4. Research Gap (RG.4): It is unsolved how to get the impedance model in a wide range of operating points with a limited set of data and how much measurement data is required to guarantee the estimation accuracy.

1.3.2. Main Objectives

This thesis intends to make improvements and find solutions to bridge the research gaps RG.1-RG.4. Correspondingly, the Ph.D. project aims to develop a technique that can accurately and efficiently measure the *dq*-frame impedance model of VSCs at a single operating point, and further propose a method for estimating the *dq*-frame impedance of VSCs over a wide range of operating points.

To fill in the identified research gaps, more specific objectives are summarized as follows

- A method of designing effective perturbation signals for the *dq*-frame impedance measurement (Obj.1).
- Analysis and mitigation method of the dynamic impact of phase angel used with *dq*-transformation on the impedance measurement results (Obj.2).
- A method of efficiently calculating the impedance matrix of VSC (Obj.3).

- A method of estimating the *dq*-frame impedance model in a wide range of operating points (Obj.4).

1.4. Research Methodology

Fig. 1.7 shows the research methodology used in this project, which are the most widely used methods in the power electronics research areas, i.e., mathematical theory, numerical simulation, and hardware experiment.

To achieve objective 1, the performance of different types of perturbation signals is analyzed and compared by using the spectrum analysis method. The small-signal modeling method is employed to investigate the mechanism of the nonlinear dynamics of VSC control, and its impact on the measurement results is also revealed by using DFT.

For the achievement of objective 2, the dynamic impact of phase angel used with *dq*-transformation on the impedance measurement is conducted by analytical calculations. Mathematical expressions are derived, which is related to the small-signal model of PLL used for the impedance measurement. The impedance measurement results are finally calculated through the DFT.

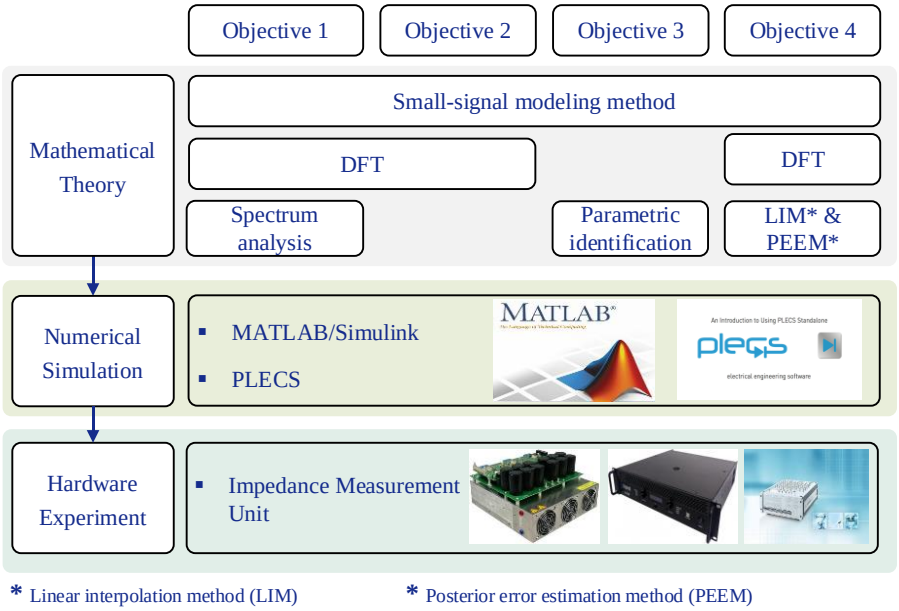

Figure 1.7. The research methodology used in the project.

For objective 3, the coupling effect of the grid impedance is investigated by the analytical expressions. The time-domain parametric identification method is utilized to identify the impedance matrix of VSC. The small-signal model of the VSC is also developed for the validation of the measurement results.

To achieve objective 4, the interpolation method is used for the estimation of the unmeasured impedance model. And the posterior error estimation method is adopted to evaluate the estimated error such that the required set of measurement data can be determined. The small-signal model of the VSC is also developed for the validation of the measurement results.

For all objectives, the verification of the theoretical analysis is generally performed in two steps. Firstly, the time-domain simulations of equivalent circuits and control diagram will be based on Simulink and PLECS, and the impedance calculation algorithms by using DFT and the time-domain parametric identification method are established, respectively. Secondly, the impedance measurement unit is built in the laboratory, which is used to validate the corresponding theoretical analysis and proposed methods in this project.

1.5. Thesis Structure

Fig. 1.8 shows the structure of the Ph.D. thesis, where the related publications are assigned to the different chapters of the thesis.

Chapter 1 introduces the background and challenges of the Ph.D. project, after which the research gap and the corresponding objective are also discussed.

Based on [C1], **Chapter 2** proposes a systematic design method for the perturbation signal, where the type of perturbation signal is chosen based on performance indexes, and frequency components of the selected perturbation signal are determined.

Based on [C2] and [J1], **Chapter 3** investigates the influence of the *dq*-transformation on the accuracy of the impedance measurement, and an improved PLL is also developed to mitigate such influence.

Based on [C3], [C4] and [J2], **Chapter 4** analyzes the coupling effect of the grid impedance on the traditional MIMO impedance calculation results, and the time-domain MIMO parametric identification method is further proposed to improve the measurement accuracy and efficiency.

Based on [J3], **Chapter 5** develops an approach to estimate the *dq*-frame impedance of three-phase VSCs at different operating points based on the multi-dimensional interpolation method. The posterior error estimation method is also adopted for the operating point intervals adjustment.

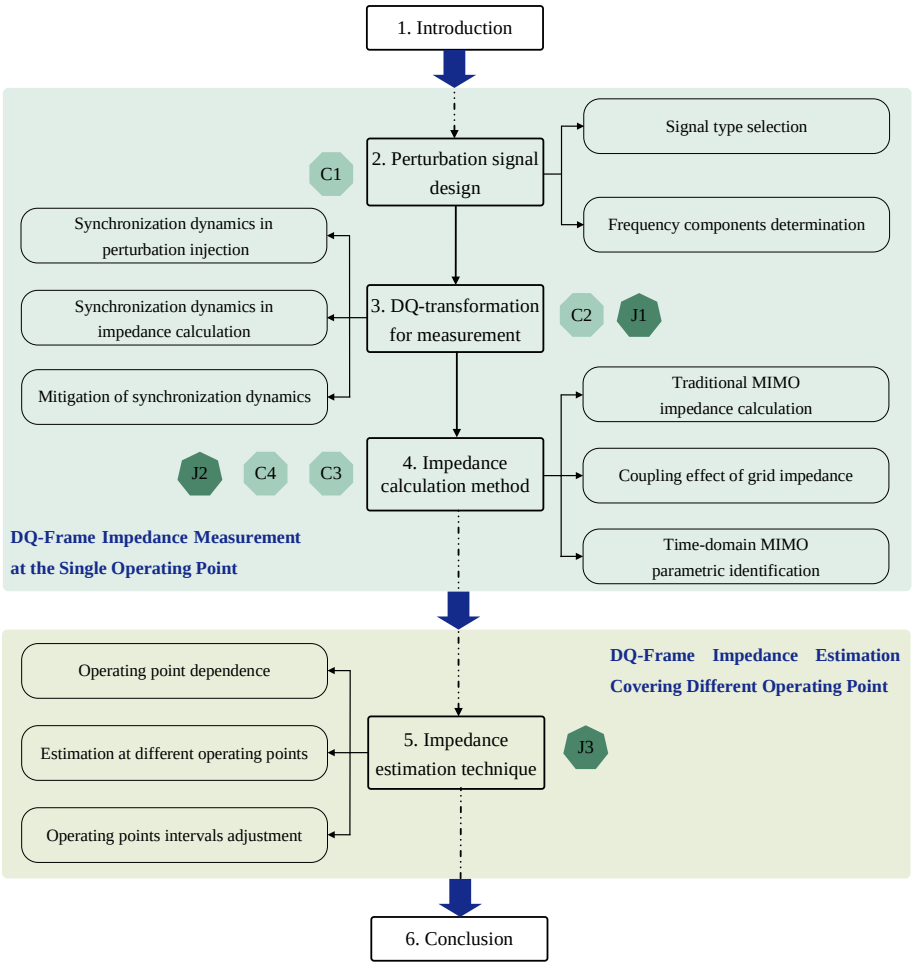

Figure 1.8. Structure of the Ph.D. thesis.

Chapter 6 summarizes the main conclusions of this thesis and gives a discussion for future work.

1.6. List of Publications

This thesis is based on the following papers in peer-reviewed conference proceedings and international journals.

Journal Papers

J1. **H. Gong**, D. Yang and X. Wang, "Impact analysis and mitigation of synchronization dynamics for DQ impedance measurement," *IEEE Trans. Power Electron.*, vol. 34, no. 9, pp. 8797-8807, Sept. 2019**.**

J2. **H. Gong**, X. Wang and D. Yang, "DQ-frame impedance measurement of three-phase converters using time-domain MIMO parametric identification, *IEEE Trans. Power Electron*., vol. 36, no. 2, pp. 2131-2142, Feb. 2021.

J3. **H. Gong**, X. Wang and D. Yang, "DQ-frame admittance estimation of three-phase converters at different operating points", *IEEE Trans. Power Electron.*, under review.

Conference Papers

C1. **H. Gong**, D. Yang and X. Wang, "Impact of nonlinear dynamics on converter DQ impedance measurement," in *Proc. IEEE 20th Workshop on Control. Model. Power Electron. (COMPEL)*, Jun, 2019, pp. 1-6.

C2. **H. Gong**, D. Yang and X. Wang, "Impact of synchronization phase dynamics on DQ impedance measurement," in *Proc. IEEE 19th Workshop on Control. Model. Power Electron. (COMPEL)*, Jun, 2018, pp. 1-7.

C3. **H. Gong**, D. Yang and X. Wang, "Parametric identification of DQ impedance model for three-phase voltage-source converters," in *Proc. IEEE Power Electron. Appl. Conf. Expo. (PEAC)*, Shenzhen, 2018, pp. 1-6.

C4. **H. Gong**, D. Yang and X. Wang, "Identification of the DQ impedance model for three-phase power converter considering the coupling effect of the grid impedance," in *Proc. IEEE Appl. Power Electron. Conf. Expo. (APEC)*, Mar, 2019, pp. 120-126.

Chapter 2. Perturbation Signal Design for DQ-Frame Impedance Measurement

The content of this chapter is based on **C1**

2.1. Introduction

This chapter presents a systematic design method for the perturbation signal used for the *dq*-frame impedance measurement, which consists of the type selection and frequency components determination of the perturbation signal. To measure the signal quality, four performance indexes are first defined. Based on these indexes, various types of wideband perturbation signals are compared under the same designed specification. With the compromise of each performance index, the type of perturbation signal is selected for the *dq*-frame impedance measurement of VSC. Then, the mechanism for the impact of nonlinear dynamics on impedance measurement results is investigated and the frequency components of the selected perturbation signal are determined to avoid such impact. Finally, Case studies are given to validate the effectiveness of the proposed method. The main content [C1] is summarized as follows.

2.2. Selection of Perturbation Signal Types

For the selection of the wideband perturbation signals, the energy density of the selected signal should be maximum in the frequency range of interest within the amplitude constraints. To give a clear guidance about the perturbation signal selection, four performance indexes are provided to measure the signal quality.

2.2.1. Definition of Different Performance Indexes

The perturbation is usually designed in the frequency-domain. Based on the discrete Fourier transform, the discrete signal $u(k)$ is represented by $U(k)$, which is written as

$$U(k) = \sum_{i=0}^{N-1} u(i)\exp(-j2\pi ki / N) \tag{2.1}$$

where N means the sequence period of the discrete signal. Therefore, the performance index for perturbation signals (PIPS) is defined as the following:

$$\mathrm{PIPS} = \frac{200\sqrt{\sum_{k=1}^{N-1}\left|U(k)\right|^2}}{N(u_{\max}-u_{\min})}\% \tag{2.2}$$

where $u_{\max}$ and $u_{\min}$ denote the maximum and minimum value, respectively. This index is not dependent on the signal scale, where 0% and 100% denote the worst and best performance, respectively.

Since the sampling frequency of the output is the same as the input, the harmonic components above the Nyquist frequency cannot be utilized for the measurement and are thus merely effective in the range of $0<k<N/2$. Thus, another index, i.e., the effective performance index (PIPSE) is defined by

$$\mathrm{PIPSE} = \frac{200}{u_{max}-u_{min}}\left(\sum_{k=1}^{R}\left|C_u^{'}(k)\right|^2\right)\% \qquad R < N/2 \tag{2.3}$$

where R represents the first nonzero harmonics that are used for the measurement; the energy density of the k^{th} harmonic in the positive frequencies is expressed as

$$\left|C_u^{'}(k)\right|^2 = \begin{cases} \left|\dfrac{U(k)}{N}\right|^2, & k=0 \\ \left|\dfrac{2\sin\pi k/N}{\pi k/N}\dfrac{U(k)}{N}\right|^2, & k>0 \end{cases} \tag{2.4}$$

Similarly, 0% and 100% denote the worst and best performance, respectively. Larger PIPSE means that the desired harmonics for the measurement contain a larger energy density, which helps improve SNR and measurement accuracy.

If only PIPSE is used as a measure of signal quality, there is a possibility that the energy density of one harmonic is low, which causes low SNR at the corresponding frequency and obtain inaccurate measurement results. To avoid this, the effective minimum ratio between the averaged amplitude and actual harmonic amplitude can be defined as

$$\mathrm{EMINE} = 100\min_{k=1,2,..R}\frac{\left|C_u^{'}(k)\right|}{\frac{1}{R}\sqrt{\left(\sum_{k=1}^{R}\left|C_u^{'}(k)\right|^2\right)}}\% \tag{2.5}$$

Compared (2.3) with (2.5), it is clear that the numerator of PIPSE is the same as the denominator of EMINE. Thus, the best performance of these two indexes cannot be

guaranteed simultaneously. Yet, since PIPSE is used for the representation of the distribution of the overall energy density while EMINE only reflects the energy density in the specified harmonics. PIPSE should be more important to make the overall measurement results accurate.

Another performance index is defined by PIPSE and EMINE, named as the time factor (TF), which is written as

$$\mathrm{TF} = 0.5\left(\frac{100}{\mathrm{PIPSE}}\right)^2\left(\frac{100}{\mathrm{EMINE}}\right)^2 \tag{2.6}$$

This index is a combination of PIPSE and EMINE, which means the required time to achieve a minimum accuracy of impedance measurement results at any of the specified harmonic from the perspective of the perturbation signal.

2.2.2. Comparison of Different Perturbation Signals

The perturbation signals are considered to be periodical and the zero-order holder is employed to produce the sequence signals with period *N*. To select the type of perturbation signal, the performance indexes of each signal are calculated and compared under the same designed specification, where the magnitude of the designed signals in the time-domain is constrained as 1, and the signals should contain 15 consecutive harmonics: f_p, $2f_p$,...$15f_p$ (f_p = 2 Hz). Table I gives the calculated performance indexes of each perturbation signal.

The multi-sine sum of harmonics (ZOHSOH) signal is first considered as the candidate perturbation signal. However, the optimization algorithm needs to minimize the peak amplitude of the signal by changing the relative phase angle of each harmonic. Fig. 2.1 shows the designed ZOHSOH in the time domain and power spectrum. It is clear that the EMINE of the signal is equal to 100%, but PIPS and PIPSE are very low due to the signal is significantly dispersed.

The discrete-interval binary signal (DIBS) is designed to strengthen as much energy as possible into the specified harmonics. Through the constant iterations, the signal is optimized to increase the EMINE. The time-domain waveform and power spectrum of designed DIBS are shown in Fig. 2.2. It is noted that EMINE of DIBS is lower than ZOHSOH while PIPSE of DIBS is higher than ZOHSOH. This means that specified harmonics of DIBS for measurement contain much more energy, which increases SNR and improves the accuracy of impedance measurement.

Pseudo-random binary sequence (PRBS) signals are generated from binary sequences of period *N*. By using appropriate feedback, the signals are easily generated through shift registers with different lengths. The designed signal is periodic, and the sequence

length is 2^m-1, where *m* represents the number of shift registers. Fig .2.3 shows the time-domain signal and power spectrum of PRBS. It is evident that no matter how well the signal is designed, some energy will be distributed on undesired frequencies. Moreover, PIPSE of PRBS is the lowest among other perturbation signals, which means desired harmonics for measurement contain less energy density.

Although the amplitude of DIBS is explicitly defined, a large amount of the energy in the nonspecified harmonics can be found. On the other hand, the ZOHSOH signals own more energy in the specified harmonics while their peak amplitude is usually much larger than a DIBS with the same designed specification. Therefore, it is feasible to utilize a multilevel multi-harmonic signal (MLMHS) to reserve the advantages of the two types of signal and simultaneously alleviate the disadvantages. A ternary MLMHS is designed, and the time-domain waveform and power spectrum are illustrated in Fig. 2.4. The designed signal has a similar performance as DIBS, which has a higher PIPSE.

Table 2.1. Performance Index of Each Perturbation Signal.

Signal Type	Levels	N	PIPSE (%)	PIPSE (%)	EMINE (%)	TF
ZOHSOH	multi	120	76.9	76.3	100	0.86
DIBS	2	120	99.9	92.1	82.6	0.86
PRBS	2	120	99.8	49.7	98.4	2.09
MLMHS	3	120	93.0	87.3	85.1	0.91

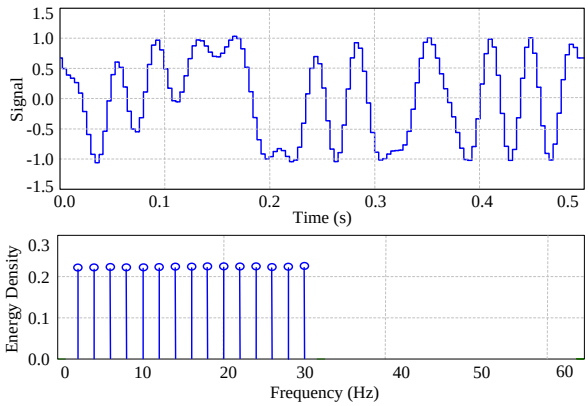

Figure 2.1. ZOHSOH signal with period N=120 PIPSE=76.3%, EMINE=100%.

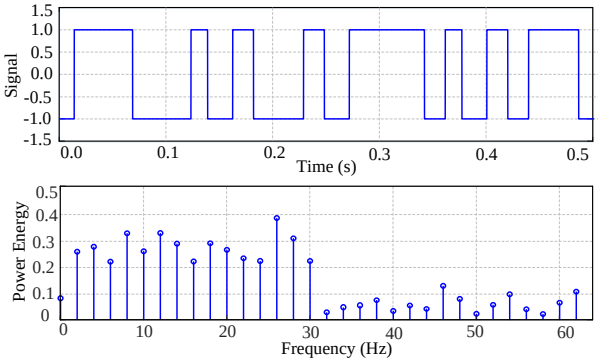

Figure 2.2. DIB signal with period N=120 PIPSE=92.1%, EMINE=82.6%.

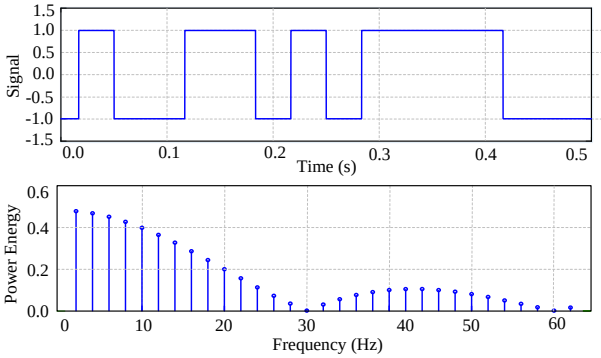

Figure 2.3. PRBS signal with period N=120 PIPSE=49.7%, EMINE=88.2%.

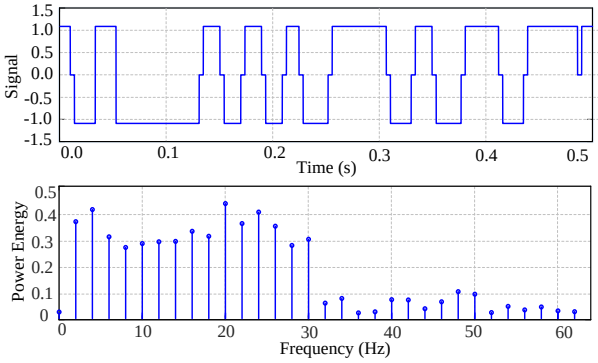

Figure 2.4. MLMHS signal with period N=120 PIPSE=87.3%, EMINE=85.1%.

It is concluded that four performance indexes of the perturbation signal cannot be guaranteed simultaneously. Thus, there is a trade-off among different performance indexes for the type design of the perturbation signal. Based on the calculated

performance indexes, DIBS can be regarded as one of the promising perturbation signals that are used for the *dq*-frame impedance measurement of VSCs.

2.3. Optimized Design of Perturbation Signal in the Presence of Nonlinear Distortions

2.3.1. Analysis of Nonlinear Dynamics

Three-phase VSC is a nonlinear-time-invariant system in the *dq*-frame, the *dq*-frame impedance model is obtained through the linearization. With the injection of wideband perturbation signals, the nonlinearity of control dynamics of VSC, which may lead to the frequency overlapping is usually overlooked. Consequently, the accuracy of the measurement results of the *dq*-frame impedance model might be influenced. The nonlinear dynamics caused by the dc voltage controller are taken as an example.

Based on the active power balance, the small-signal model of the dc voltage control can be obtained through the linearization around the operating point, which can be written as

$$sC_{dc}(U_{dc0}\Delta U_{dc}+\frac{\Delta U_{dc}^{2}}{2})=E_{d0}\Delta i_d+I_{d0}\Delta E_d+E_{q0}\Delta i_q+I_{q0}\Delta E_q+\Delta E_d\Delta i_d+\Delta E_q\Delta i_q \tag{2.7}$$

where E_{dq0}, I_{dq0} represent the steady-state values of *dq*-axis voltage and current, respectively. U_{dc0} and C_{dc} are the dc voltage and capacitor. To measure the *dq*-frame impedance model, the amplitude of the injected perturbation signal is usually chosen at 5%-10% of the steady-state values. Thus, the multiplied terms $\triangle U_{dc}^{2}$, $\triangle E_d\triangle i_d$, and $\triangle E_q\triangle i_q$, i.e., nonlinear responses might be relatively large such that its impact on the impedance measurement cannot be ignored.

Given the single-frequency perturbation signal at ω_p, the multiplication of perturbation terms yields infinite harmonics of voltage and current in the closed-loop control system, which can be written as

$$\begin{aligned}\Delta E_d\Delta i_d &= U_p\cos(\omega_p t)[I_{p1}\cos(\omega_p t)+I_{p2}\cos(2\omega_p t)+...]\\ &=\frac{U_p}{2}[I_{p_1}\cos(2\omega_p t)-I_{p_1}\cos(0t)+I_{p2}\cos(\omega_p t)+...]\end{aligned} \tag{2.8}$$

Fig. 2.5 shows the power spectrum of the *d*-axis current with the injection of a single-frequency perturbation signal at ω_p. It is clear that *d*-axis current response contains multiple harmonic components even the perturbation signal is only injected at one

frequency point, where the blue bar represents the response of $\Delta I_d^{f_p}$ at the injected frequency f_p while the red bars mean the frequency coupling components of $\Delta I_d^{f_c}$ caused by the nonlinear dynamics at $2f_p$, $3f_p$, $4f_p$…..

Given the wideband perturbation signal (DIBS), it can be expressed as

$$U_p(t) = \sum_{n=1,2,3...}^{N} U_{pn} \cos(n\omega_p t + \varphi_n) \tag{2.9}$$

In this case, one of the multiplication terms can be calculated as

$$\begin{aligned} \Delta E_d \Delta i_d &= \sum_{n=1,2,3...}^{N} U_{pn} \cos(n\omega_p t + \varphi_n) \times \sum_{m=1,2,3...}^{N} I_{pm} \cos(m\omega_p t + \phi_m) \\ &= \sum_{n=1,2,3..}^{N} \sum_{m=1,2,3..}^{N} \frac{U_{pn} I_{pm}}{2} \cos[(m \pm n)\omega_p t + (\varphi_n \pm \phi_m)] \end{aligned} \tag{2.10}$$

According to equation (2.10), the multiplication term leads to nonlinear dynamics, which makes the voltage and current contain multi-frequency components. Thus, there exists frequency overlapping between the injected components $\Delta I_d^{f_{p1,2,3..}}$ and coupling components $\Delta I_d^{f_{c1,2,3..}}$, if the wideband perturbation signal is injected. Fig. 2.6 illustrates the spectrum of the *d*-axis current. The responses contributed from the injected components are integrated with the coupling responses, which will affect the measurement results of the *dq*-frame impedance model.

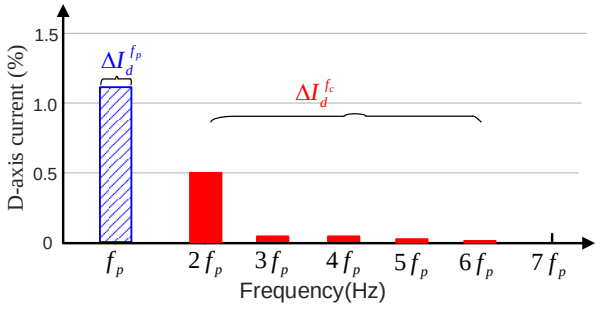

Figure 2.5. The power spectrum of *d*-axis current with the injection of a sinusoidal signal. Source: [C1].

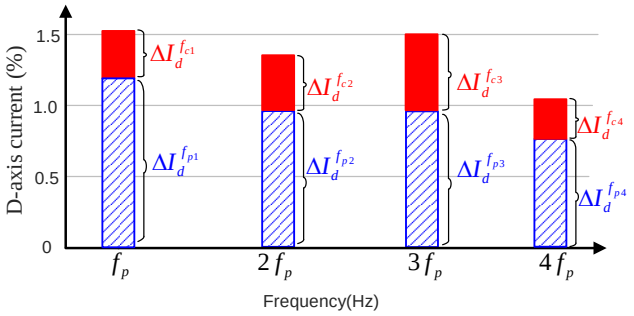

Figure 2.6. The power spectrum of the *d*-axis with the injection of wideband perturbation signal. Source: [C1].

2.3.2. Optimized Design of Perturbation Signal

In order to mitigate the frequency overlapping caused by the injection of the wideband perturbation signal, the perturbation signal should be further optimized. As shown in (2.9), the injected perturbation signal is consist of f_p, $2f_p$, $3f_p$….. However, if we only consider the multiplication of voltage and current at the injected frequency component, it means that *m* equal to *n*, as shown in (2.10). It can be further found that the responses caused by the nonlinear dynamics are consist of even harmonics ($2n\omega_p$ or $2m\omega_p$). Therefore, the injected perturbation signal is designed to only contain odd harmonics: f_p, $3f_p$, $5f_p$, $7f_p$……, as shown in (2.9)

$$\Delta U_{pd}(t) = \sum_{n=1,3,5...}^{N} U_{pn} \cos(n\omega_p t) \tag{2.11}$$

The corresponding nonlinear term can be expressed by

$$\Delta E_d \Delta i_d = \sum_{n=1,3,5..}^{N} \sum_{n=1,3,5..}^{N} \frac{U_{pn} I_{pn}}{2} \cos[(n \pm n)\omega_p t + (\varphi_n \pm \phi_m)] \tag{2.12}$$

As shown in Fig. 2.7, the responses contributed from the injected components are odd harmonics, which can be distinguished from the coupling responses caused by the nonlinear dynamics (even harmonics). Therefore, accurate measurement results can be obtained.

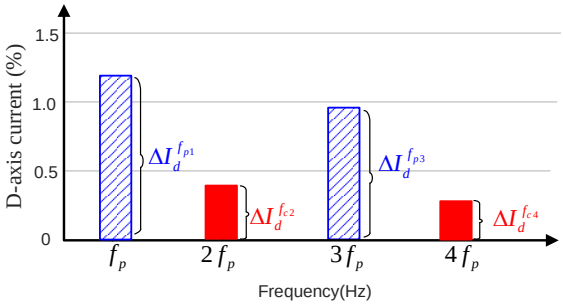

Figure 2.7. The power spectrum of *d*-axis current with the injection of wideband perturbation injection. Source: [C1].

2.4. Case Study

To validate the effectiveness of the designed perturbation signal, an impedance measurement setup is built for the case study. The frequency range for the measurement is 2 Hz - 30 Hz and the analytical model is calculated for the validation of the measurement results.

Four different types of perturbation signals, as designed in Table I, are used for the impedance measurement. Fig. 2.8 illustrates the impedance measurement results by using those designed perturbation signals, where the noise is not introduced in the measurement. It is clear that all impedance measurement results match well with the theoretical model when using different types of perturbation signals.

Fig. 2.9 gives the impedance measurement results when utilizing four different perturbation signals, where 5% of white noise is intentionally introduced in the measurement. For the perturbation signal of Sine, the overall measurement result is accurate to some extent since the energy density is evenly distributed at each frequency. The result measured via PRBS agrees well with the theoretical result below 15 Hz while it does not match with the theoretical model from 15 Hz to 30 Hz. This is because the energy density of PRBS decreases as the frequency increases such that the response submerges into the noise. The measurement results obtained by using DIBS and MLMHS match well with the theoretical model. Compared with Fig. 2.8, the purpose of the perturbation signals selection is to find an appropriate signal that has high energy density at the frequency range of interest so that the impact of the noise on the measurement can be minimized.

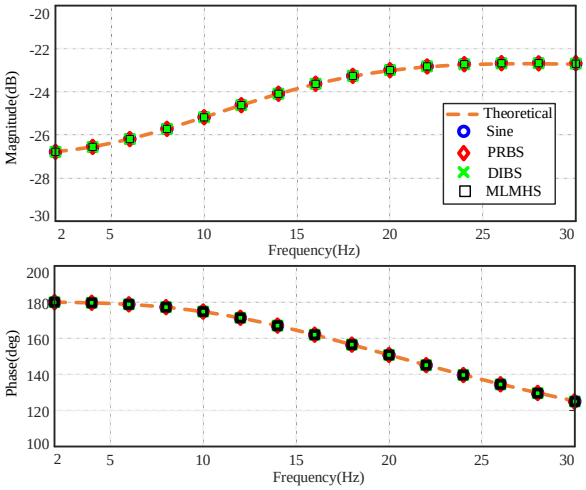

Figure 2.8. Impedance measurement results by using different perturbation signals without considering noise.

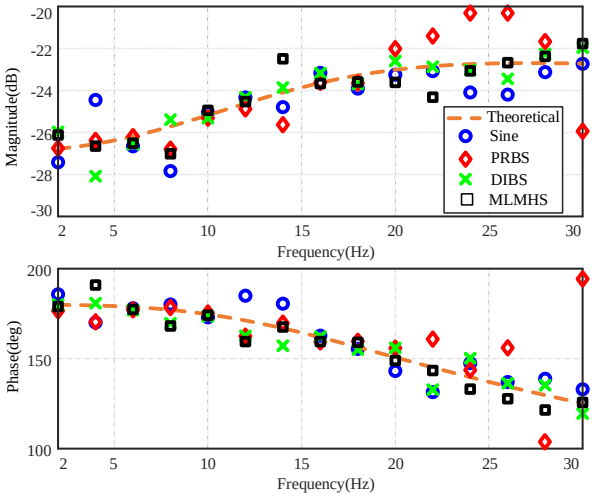

Figure 2.9. Impedance measurement results by using different perturbation signals with white noise.

Based on calculated performance indexes, the DIBS is chosen as the injected perturbation signal utilized for the *dq*-frame impedance measurement of VSCs. To investigate the impact of the nonlinear dynamics of VSC control, the sinusoidal signal is first injected. Fig. 2.9 illustrates the measured *dq*-axis currents and voltages without injecting the perturbation signal. It can be seen from the DFT analysis that there exist background harmonics (50 Hz and 100 Hz). Fig. 2.10 depicts the measured *dq*-axis output current and voltage when a 10 Hz sinusoidal signal is injected. It is clear that the current responses not only include the injected components at 10 Hz but also

contain the frequency-coupling components, for instance, 20 Hz, 30 Hz, etc. Fig. 2.11 gives measured *dq*-axis output current and voltage when 10 Hz and 20 Hz components are simultaneously injected. Compared with Fig. 2.10, it can be seen that the injection of perturbation signal leads to the frequency-coupling response, which further causes the frequency-overlapping (such as the components at 20 Hz) and affects the accuracy of impedance measurement results if the wideband perturbation signal is injected.

Fig. 2.13 and 2.14 shows the measurement results of Y_{dd} and Y_{qq}, where the traditional perturbation signal and the intentionally designed perturbation signal are used for the measurement. It is clear that the intentionally designed perturbation signal can obtain accurate *dq*-frame impedance measurement results while the measurement results obtained from the traditional perturbation signal do not match with the analytical model, especially in the low-frequency range. This phenomenon is due to the fact that the nonlinear dynamics cause frequency-overlapping when the traditional wideband perturbation is injected.

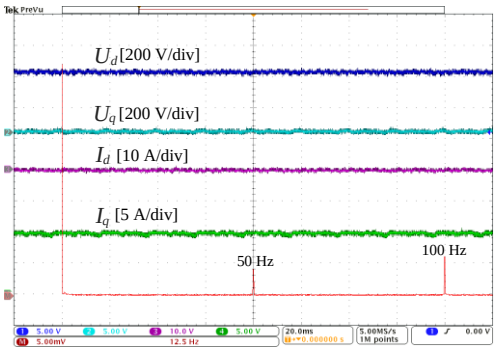

Figure 2.10. DQ-axis current and voltage when there is no perturbation signal injected into the system. Source: [C1].

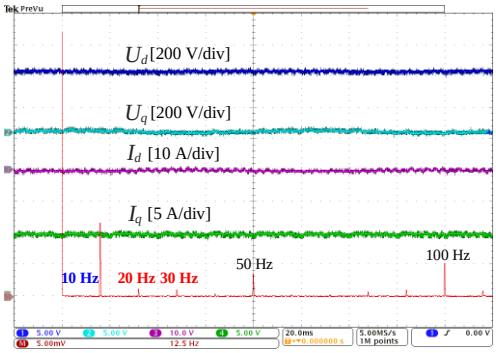

Figure 2.11. DQ-axis current and voltage when a 10 Hz sinusoidal signal is injected into the system. Source: [C1].

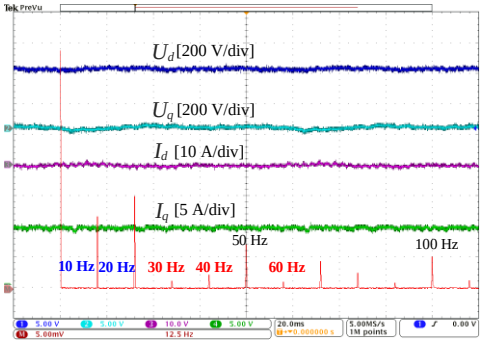

Figure 2.12. DQ-axis current and voltage when a 10 Hz and 20 Hz multi-sinusoidal signal is injected into the system. Source: [C1].

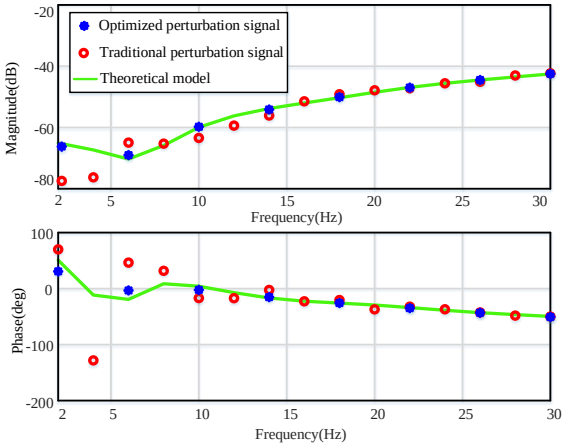

Figure 2.13. Impedance measurement results of Y_{dd} by using the optimized perturbation signal.

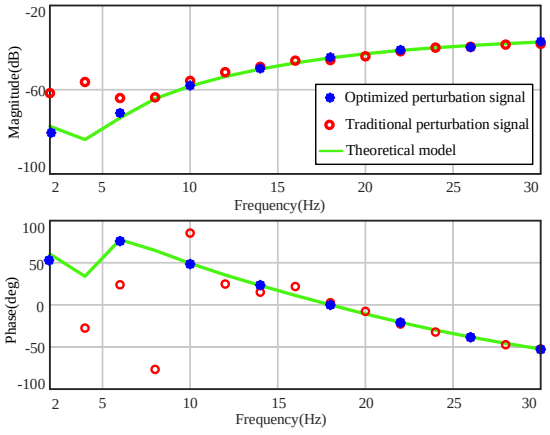

Figure 2.14. Impedance measurement results of Y_{qq} using the optimized perturbation signal.

More detailed discussions and case studies can be found in [C1].

2.5. Summary

This chapter develops a systematic method of designing effective perturbation signals for the *dq*-frame impedance measurement of VSCs. The approach first evaluates different types of perturbation signals based on defined performance indexes. It is revealed that there is a trade-off for the type selection of perturbation signals. To avoid the impact of frequency-overlapping caused by nonlinear dynamics of VSC control on the *dq*-frame impedance measurement, the selected perturbation signal is further optimized to determine the injected frequency components. The theoretical analysis is verified by the simulation tests.

Chapter 3. Impact of DQ-Transformation on Impedance Measurement

The content of this chapter is based on **J**1 and **C**2

3.1. Introduction

This chapter presents a comprehensive analysis of the dynamic impact of the phase angle used with *dq*-transformation on the accuracy of the *dq*-frame impedance measurement results, and a mitigation method of such impact is also proposed. First, the impact of synchronization dynamics on the impedance measurement is separately investigated, which is the dynamic impact on the perturbation injection and the dynamic impact on the impedance calculation. Then, an approach for the mitigation of the synchronization dynamics caused by both PLL and variation of the fundamental frequency is proposed. Lastly, the experiment results are given to verify the theoretical analysis. The main content of [J1] and [C2] is summarized as follows.

3.2. Synchronization Dynamics Impacts on Perturbation Injection and Impedance Calculation

To clearly explain the dynamic impact of the phase angle used with *dq*-transformation on the impedance measurement, the corresponding effects are divided into two parts: the perturbation injection and impedance calculation.

3.2.1. Synchronization Dynamics Impact on Perturbation Injection

Fig. 3.1 illustrates three *dq*-frames which are separately aligned with the PCC-voltage

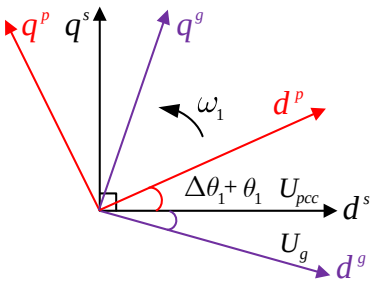

Figure 3.1. Three *dq*-frames which are aligned with the PCC-, perturbation- and grid-voltage, respectively. Source: [J1].

perturbation-voltage and grid voltage. It is first assumed that the synchronization phase angle utilized for the impedance calculation is accurate, which is exactly the PCC-voltage *dq*-frame. θ_p represents the synchronization phase angel aligned for the perturbation-voltage and θ_s is used for the PCC-voltage *dq*-frame. $\triangle\theta_1+\theta_1$ is the angle difference between θ_s and θ_p, where the phase dynamic $\triangle\theta_1$ is caused by the PLL, and θ_1 denotes the initial phase of the perturbation voltage. The composition of the injected perturbation components on the *d*-axis and *q*-axis is determined by θ_1. Based on the transformation of two *dq*-frames, the perturbation components $U^{\,p}_{pd,q}$ injected on the perturbation-voltage *dq*-frame can be expressed in the PCC-voltage *dq*-frame by:

$$\begin{bmatrix} U^{\,s}_{pd0}+U^{\,s}_{pd} \\ U^{\,s}_{pq0}+U^{\,s}_{pq} \end{bmatrix} = \begin{bmatrix} \cos(\theta_1+\Delta\theta_1) & \sin(\theta_1+\Delta\theta_1) \\ -\sin(\theta_1+\Delta\theta_1) & \cos(\theta_1+\Delta\theta_1) \end{bmatrix} \begin{bmatrix} U^{\,p}_{pd0}+U^{\,p}_{pd} \\ U^{\,p}_{pq0}+U^{\,p}_{pq} \end{bmatrix} \tag{3.1}$$

where $U^{\,p}_{pd0,q0}$ and $U^{\,s}_{pd0,q0}$ means the perturbation steady-state values injected on the perturbation- and PCC-voltage *dq*-frame, respectively. Since they are equal to zero, the synchronization dynamics introduced by PLL is prevented. Thus, the accuracy of the measured impedance results is not affected even if different bandwidths of PLL are employed to calculate the synchronization phase angle for the injection of the perturbation signal.

The measured voltage and current response can be expressed in the perturbation- and PCC-voltage *dq*-frame as

$$\begin{bmatrix} U^{\,s}_{pd} \\ U^{\,s}_{pq} \end{bmatrix} = \begin{bmatrix} \cos\theta_1 & \sin\theta_1 \\ -\sin\theta_1 & \cos\theta_1 \end{bmatrix} \begin{bmatrix} U^{\,p}_{pd} \\ U^{\,p}_{pq} \end{bmatrix} \qquad \begin{bmatrix} I^{\,s}_{pd} \\ I^{\,s}_{pq} \end{bmatrix} = \begin{bmatrix} \cos\theta_1 & \sin\theta_1 \\ -\sin\theta_1 & \cos\theta_1 \end{bmatrix} \begin{bmatrix} I^{\,p}_{pd} \\ I^{\,p}_{pq} \end{bmatrix} \tag{3.2}$$

Based on equation (3.2), the measured admittance $\mathbf{Y}^{\boldsymbol{m}}_{\boldsymbol{dq}}$ can be calculated as

$$\mathbf{Y}^{\boldsymbol{m}}_{\boldsymbol{dq}} = \begin{bmatrix} \cos\theta_1 & \sin\theta_1 \\ -\sin\theta_1 & \cos\theta_1 \end{bmatrix} \mathbf{Y}^{\boldsymbol{p}}_{\boldsymbol{dq}} \begin{bmatrix} \cos\theta_1 & \sin\theta_1 \\ -\sin\theta_1 & \cos\theta_1 \end{bmatrix}^{-1} = \mathbf{Y}^{\mathbf{s}}_{\boldsymbol{dq}} \tag{3.3}$$

where $\mathbf{Y}^{s}_{\boldsymbol{dq}}$ is the actually desired admittance in the PCC-voltage *dq*-frame. Therefore, it can be seen that the initial phase for the perturbation injection does not affect the accuracy of measurement results.

3.2.2. Synchronization Dynamics Impact on Impedance Calculation

Fig. 3.2 illustrates three *dq*-frames aligned with PCC- and measured-voltages with the injection of two linearly independent perturbations. The real phase angle of the PCC voltage is represented by θ and the synchronization phase angle estimated by PLL is θ_m. Since the PLL would introduce the dynamics in the impedance calculation, the angle differences between θ and θ_m might appear, which can be denoted by $\triangle\theta$ and $\triangle\theta'$, respectively. Thus, the measured voltages in the PCC-voltage *dq*-frame (superscript's') are expressed in the measured-voltage *dq*-frame (superscript 'm') as

$$\begin{bmatrix} U^m_{pd1} \\ U^m_{pq1} \end{bmatrix} = \begin{bmatrix} \cos(\Delta\theta) & \sin(\Delta\theta) \\ -\sin(\Delta\theta) & \cos(\Delta\theta) \end{bmatrix} \begin{bmatrix} U^s_{pd1} \\ U^s_{pq1} \end{bmatrix} \quad \begin{bmatrix} U^m_{pd2} \\ U^m_{pq2} \end{bmatrix} = \begin{bmatrix} \cos(\Delta\theta') & \sin(\Delta\theta') \\ -\sin(\Delta\theta') & \cos(\Delta\theta') \end{bmatrix} \begin{bmatrix} U^s_{pd2} \\ U^s_{pq2} \end{bmatrix} \tag{3.4}$$

The synchronization phase dynamics are denoted by the closed-loop transfer function of PLL, G_{PLL}. Thus, equation (3.4) can be re-written as

$$\begin{bmatrix} U^m_{pd1} & U^m_{pd2} \\ U^m_{pq1} & U^m_{pq2} \end{bmatrix} = \begin{bmatrix} 1 & U^s_{q0} G_{PLL} \\ 0 & 1 - U^s_{d0} G_{PLL} \end{bmatrix} \begin{bmatrix} U^s_{pd1} & U^s_{pd2} \\ U^s_{pq1} & U^s_{pq2} \end{bmatrix} \tag{3.5}$$

Similarly, the measured current responses in two different *dq*-frames can be also obtained based on equation (3.5). Consequently, the relationship between the real admittance matrix $\mathbf{Y}^s_{dq}$ and the measured admittance matrix $\mathbf{Y}^m_{dq}$ can be expressed as

$$\mathbf{Y}^m_{dq} = \left(\mathbf{Y}^s_{dq} + \begin{bmatrix} 0 & I^s_{q0} G_{PLL} \\ 0 & -I^s_{d0} G_{PLL} \end{bmatrix} \right) \cdot \begin{bmatrix} 1 & U^s_{q0} G_{PLL} \\ 0 & 1 - U^s_{d0} G_{PLL} \end{bmatrix}^{-1} \tag{3.6}$$

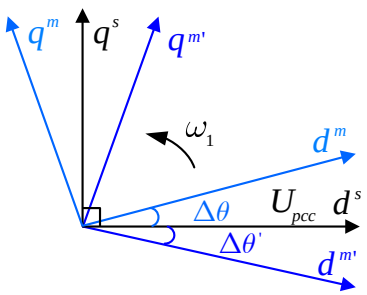

Figure 3.2. Three *dq*-frames aligned with PCC- and measured-voltages, respectively. Source: [J1].

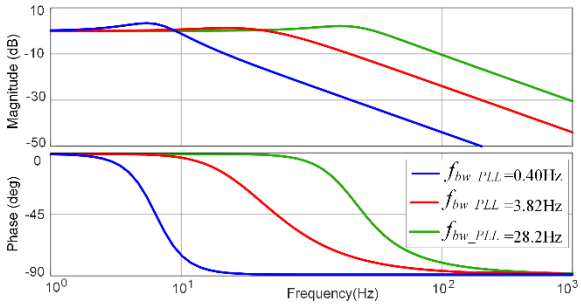

Figure 3.3. The frequency response of the closed-loop transfer functions of the PLL. Source: [J1].

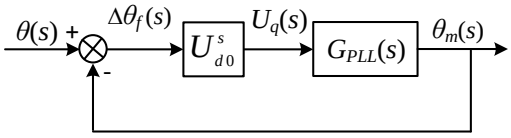

Figure 3.4. The Block diagram of the small-signal model of PLL. Source: [J1].

It is noted that there exists a discrepancy between the real admittance matrix and the measured admittance matrix due to the impact of the synchronization dynamics introduced by PLL.

Fig. 3.3 illustrates the frequency response of the transfer function $U_{d0}^s G_{PLL}$ under different bandwidths of PLL. It can be seen that PLL acts as a low-pass filter (LPF). When the frequencies of the injected perturbation signal are smaller than the cut-off frequency of LPF, i.e., the bandwidth of the PLL, the synchronization dynamics may result in a significant impact on the measurement results of the *dq*-frame impedance model. It is, therefore, suggested to design the PLL whose bandwidth is extremely lower than the lowest frequency of the injected perturbation signal.

3.3. Mitigation of Synchronization Dynamics for Impedance Measurement

Fig. 3.4 illustrates the block diagram of the small-signal model of PLL. The phase angle difference between the PLL-calculated angle and PCC voltage angle is represented by $\Delta\theta_f$, which is due to the existence of frequency variation. It can be expressed as:

$$\Delta\theta_f(s) = \frac{1}{1 + U_{d0}^s G_{PLL}(s)} \cdot \theta(s) \tag{3.7}$$

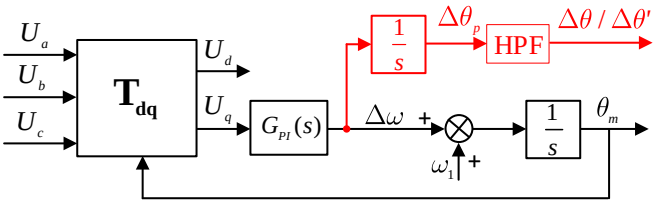

Figure 3.5. The improved PLL for the impedance calculation. Source: [J1].

Based on the final theorem, the steady-state error of phase difference $\triangle\theta_f$ is derived as

$$\Delta\theta_f = \lim_{t\to\infty} e(t) = \lim_{s\to 0} s\Delta\theta_f(s) = \frac{2\pi K_{ramp}}{U^s_{d0} K_{PLL\_i}} \tag{3.8}$$

where K_{ramp} denotes the ramp rate of frequency deviation and K_{PLL_i} represents the integral gain of PLL. In this case, there exist discrepancies between the measured voltage and real voltage, which can be written as

$$\begin{bmatrix} U^m_{pd1} \\ U^m_{pq1} \end{bmatrix} = \begin{bmatrix} \cos(\Delta\theta_f) & \sin(\Delta\theta_f) \\ -\sin(\Delta\theta_f) & \cos(\Delta\theta_f) \end{bmatrix} \begin{bmatrix} U^s_{pd1} \\ U^s_{pq1} \end{bmatrix} \tag{3.9}$$

To alleviate the negative effects of the phase difference $\triangle\theta_f$ caused by frequency change, the PLL bandwidth should be designed higher.

There is a trade-off between the selections of the PLL bandwidth: a higher bandwidth of PLL is preferred to track the system frequency changes while it introduces the synchronization dynamics on the measured voltage and current responses, and consequently influences the impedance calculation results. Fig. 3.5 illustrates the diagram of the improved PLL used for the impedance measurement. The synchronization phase dynamics $\triangle\theta$ and $\triangle\theta'$ are extracted to correct the measured voltage and current response, which can be expressed by

$$\begin{bmatrix} U^s_{pd1} \\ U^s_{pq1} \end{bmatrix} = \begin{bmatrix} \cos(\Delta\theta) & \sin(\Delta\theta) \\ -\sin(\Delta\theta) & \cos(\Delta\theta) \end{bmatrix}^{-1} \begin{bmatrix} U^m_{pd1} \\ U^m_{pq1} \end{bmatrix} \quad \begin{bmatrix} I^s_{pd1} \\ I^s_{pq1} \end{bmatrix} = \begin{bmatrix} \cos(\Delta\theta) & \sin(\Delta\theta) \\ -\sin(\Delta\theta) & \cos(\Delta\theta) \end{bmatrix}^{-1} \begin{bmatrix} I^m_{pd1} \\ I^m_{pq1} \end{bmatrix} \tag{3.10}$$

Based on equation (3.10), accurate admittance can be calculated from the compensated voltage and current responses.

3.4. Experiment Validation

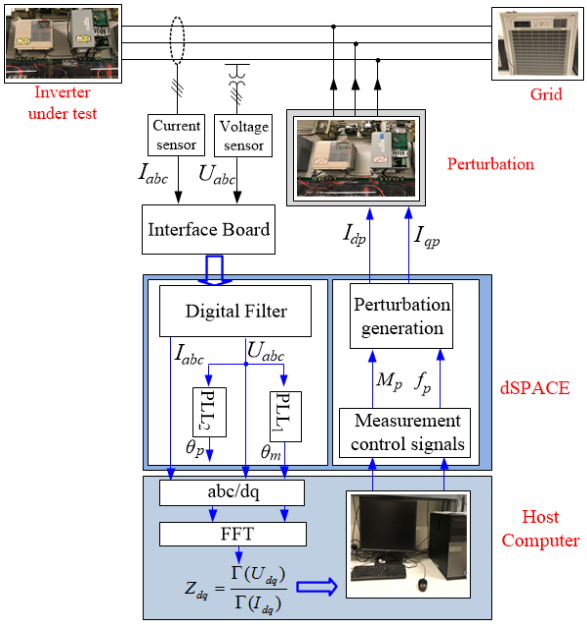

Figure 3.6. The experiment setup of the impedance measurement system. Source: [J1].

Table 3.1. Controller and Circuit Parameters of the Measured VSC. Source: [J1].

Symbol	Description	Value
K_{i_p}/K_{i_i}	Current inner controller	6/1000
K_p/K_i	PI controller of PLL	0.47/44.4
ω	Grid frequency	314 rad/s
f_s	Sampling frequency	10 kHz
I_{d0}/I_{q0}	*dq* channel current steady value	8 A/ 0 A
U_{d0}/U_{q0}	*dq* channel voltage steady value	400 V/ 0 V
U_{dc0}	DC voltage of the converter	730 V
U_g	Grid phase-neutral peak voltage	325 V
L	Filtered inductor	1.5 mH
C_g	Grid capacitor	15 μF
T_d	Deadtime	2 μs
L_g	Grid inductor	7.5 mH

In this part, experimental tests are carried out to verify the accuracy of theoretical analysis. The experiment setup is shown in Fig. 3.6, where two Danfoss converters are adopted. One converter is the tested object and the other is considered as the perturbation source. Table 3.1 gives the parameters of the converter under test. When the converter operates in the high power factors, the magnitude of Y_{dq} and Y_{qd} are much smaller than the admittance of Y_{dd} and Y_{qq}. For simplicity, only the measured results of Y_{dd} and Y_{qq} are given for validation.

3.4.1. Synchronization Dynamics in Perturbation Injection

Table 3.2. Influence Factors for Perturbation Injection. Source: [J1].

Case	ROCOF	PLL parameters: K_{PLL_p}/K_{PLL_i}	Bandwidth	Initial Phase
Case 1	0.0 Hz/s	0.47/44.4	28.2 Hz	0°
Case 2	0.0 Hz/s	0.47/44.4	28.2 Hz	90°
Case 3	0.0 Hz/s	0.03/0.20	2.0 Hz	90°
Case 4	0.5 Hz/s	0.47/44.4	28.2 Hz	90°

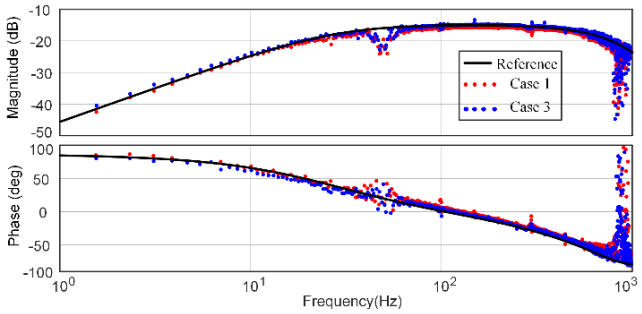

(a)

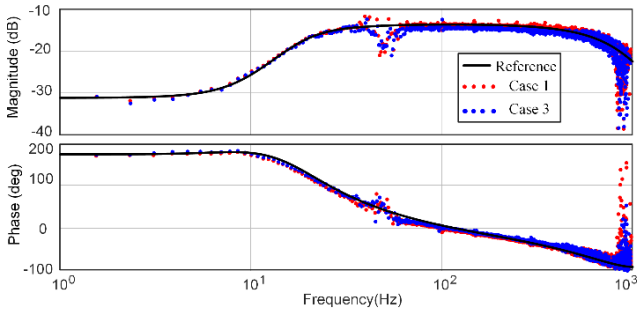

(b)

Figure 3.7. Measured admittance model when different synchronization angles are used for the injection of perturbation. (a) Y_{dd}. (b) Y_{qq}. Source: [J1].

Table 3.2 gives four designed cases, where different initial phases and bandwidths of PLL are adopted for the perturbation injection. In the experiment test, only Case 1 and Case 3 are selected for validation. Fig.3.7 illustrates the measured admittance of Y_{dd} and Y_{qq} under different synchronization phase angles for the perturbation injection. It is proved that the initial phase angle and bandwidth of PLL do not affect the accuracy of the measured results.

3.4.2. Synchronization Dynamics in Impedance Calculation

Table 3.3. Different Bandwidths of PLL. Source: [J1].

Case	ROCOF	PLL parameters: K_{PLL_p}/K_{PLL_i}	Bandwidth
Case 5	0.0 Hz/s	0.01/0.04	0.4 Hz
Case 6	0.0 Hz/s	0.03/0.20	2.0 Hz
Case 7	0.0 Hz/s	0.47/4.44	9.5 Hz
Case 8	0.0 Hz/s	0.47/44.4	28.2 Hz

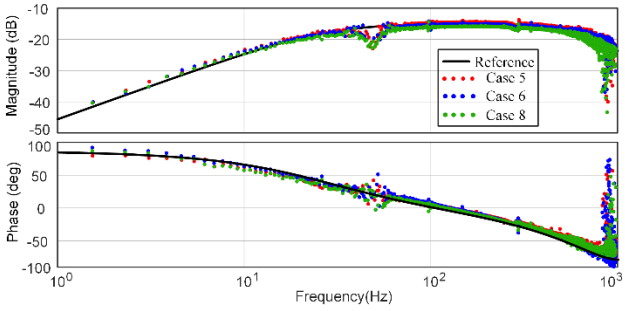

(a)

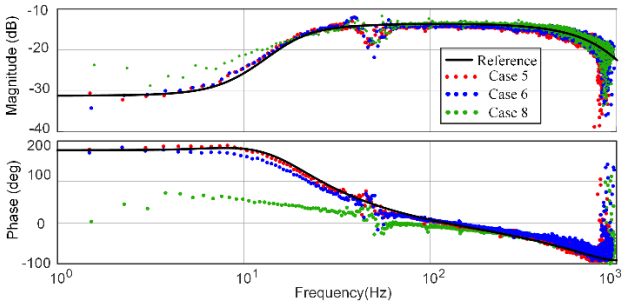

(b)

Figure 3.8. Measured admittance model when using different bandwidths of PLL for impedance calculation. (a) Y_{dd}. (b) Y_{qq}. Source: [J1].

Table 3.3 gives four designed cases, where different bandwidths of PLL are employed to estimate the phase angle for the impedance calculation. In Case 5 and Case 8, the bandwidths of PLL are designed to be extremely lower and higher than the lowest injected frequency components (1.9 Hz), respectively. In Case 6, the designed bandwidth of PLL is approximate to 1.9 Hz. Correspondingly, Fig. 3.8 illustrates the measured admittance of Y_{dd} and Y_{qq} in these three cases. It is concluded that synchronization dynamics only affect the measured result of Y_{qq}, and lower bandwidth of PLL is desired to mitigate the impact and yield accurate results.

3.4.3. Impact of Frequency Variations on Impedance Calculation

Table 3.4 Influence of Frequency Variations. Source: [J1]

Case	ROCOF	PLL parameters: K_{PLL_p}/K_{PLL_i}	Bandwidth
Case 9	0.5 Hz/s	0.01/0.04	0.4 Hz
Case 10	0.5 Hz/s	0.10/1.0	4.4 Hz
Case 11	5.0 Hz/s	0.10/1.0	4.4 Hz
Case 12	5.0 Hz/s	0.47/44.4	28.2 Hz

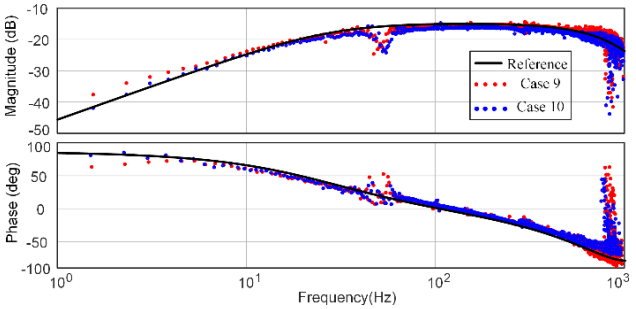

(a)

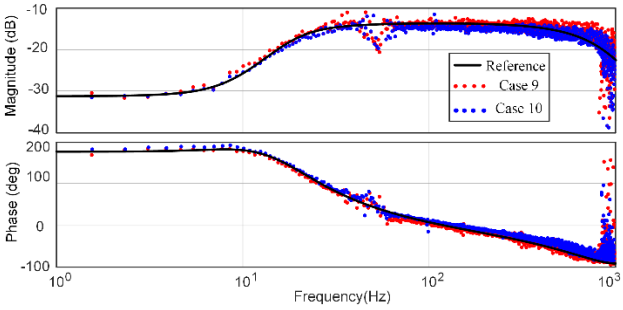

(b)

Figure 3.9. Measured admittance model with the variation of system frequency when using different bandwidths of PLL. (a) Y_{dd}. (b) Y_{qq}. Source: [J1].

Table 3.4 gives four different cases, where different rates of the frequency changes (ROCOFs) of the system and bandwidths of PLL are adopted. Corresponding, Fig. 3.9 illustrates the measured admittance of Y_{dd} and Y_{qq} in Case 9 and Case 10. When the system frequency varies, an extremely lower bandwidth of PLL cannot accurately track the synchronization phase angle of the PCC voltage, which further results in the discrepancy between the measured admittance and the theoretical admittance model.

3.4.4. Measurement Comparison between Different Methods

Table 3.5. Different Measurement Methods. Source: [J1].

Case	ROCOF	PLL parameters: K_{PLL_p}/K_{PLL_i}	Synchronization Phase Estimation
Case 13	0.5 Hz/s	0.47/44.4	Traditional PLL
Case 14	0.5 Hz/s	0.47/44.4	Proposed method in [15]
Case 15	0.5 Hz/s	0.47/44.4	Proposed method

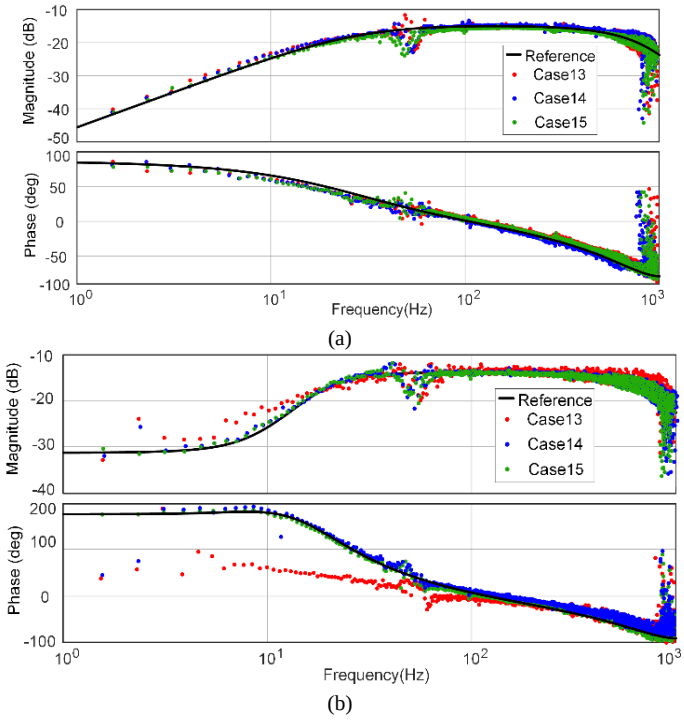

Figure 3.10. Measured admittance based on different measurement methods. (a) Y_{dd}. (b) Y_{qq}. Source: [J1].

Table 3.5 gives three cases, where different estimation methods of the synchronization phase are used. Fig. 3.10 illustrates the measured admittance of Y_{dd} and Y_{qq} by using different estimation methods. It is proved that the traditional method yields the inaccurate result of Y_{qq} while the approach developed in [39] can get accurate results in a wide frequency range. When using the proposed estimation method in the paper, the measured results match well with the theoretical model.

More detailed discussions and case studies can be found in [J1] and [C2].

3.5. Summary

This chapter analyzes the dynamic impact of the phase angle used with the *dq*-transformation on the impedance measurement. It is revealed that the synchronization dynamics in the impedance calculation significantly affect the accuracy of measurement results while the synchronization dynamics in the perturbation injection rarely affect the impedance measurement. To mitigate the impact and obtain accurate results, an improved PLL is proposed for the impedance measurement. The experimental results have proved the theoretical analysis and the effectiveness of the proposed method.

Chapter 4. Calculation Method for DQ-Frame Impedance Measurement

The content of this chapter is based on **J2**, **C**3 and **C4**.

4.1. Introduction

This chapter develops a time-domain MIMO parametric identification method for the impedance calculation, which can effectively calculate the *dq*-frame impedance matrix of VSC and simultaneously eliminate the coupling effects of the grid impedance on measurement results. The conventional MIMO *dq*-frame impedance calculation method for VSCs is first discussed, and the impact of the grid impedance on the traditional MIMO impedance calculation results is then investigated. Further, the basic principle of the time-domain MIMO parametric impedance identification method is briefly explained and the implementation procedure of this method is explicitly presented. Lastly, the experiment results are given to validate the effectiveness of the proposed method. The main content of [J2], [C3] and [C4] is summarized as follows.

4.2. Traditional MIMO Impedance Measurement of VSCs in the DQ-Frame

Fig. 4.1 shows the configuration of the traditional MIMO impedance measurement technique. It consists of two parts: perturbation injection and impedance calculation. For the perturbation injection, two uncorrelated excitation signals are injected into the measurement system at the same time. Therefore, two wideband excitation signals, i.e., Pseudo-Random Binary (PRBS), are designed with different frequency points to sufficiently perturbing the MIMO system. Fig. 4.2 shows the time-domain waveforms and power spectrum of the two designed PRBSs, where the energy density of two PRBSs do not coincide with each other.

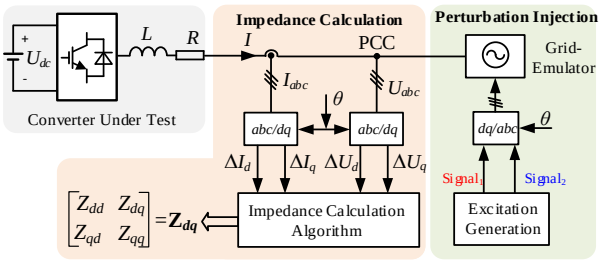

Figure 4.1. Configuration of the traditional MIMO impedance measurement technique. Source: [J2].

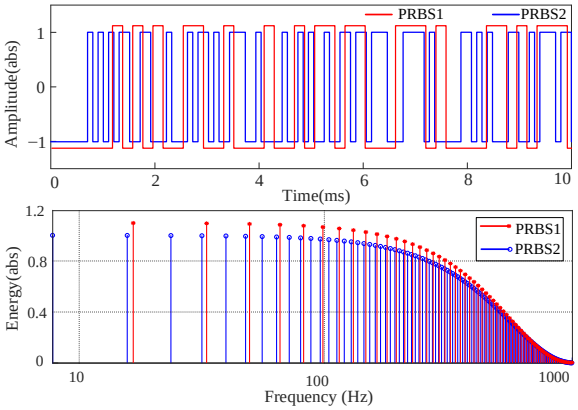

Figure 4.2. Time-domain waveforms and power spectrum of two uncorrelated PRBSs. Source: [J2].

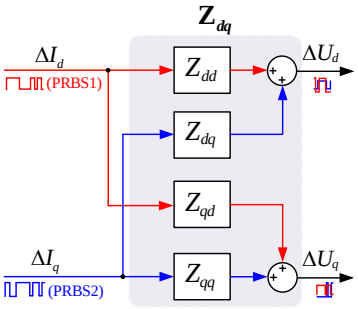

Figure 4.3. Traditional MIMO impedance calculation method without the impact of the grid impedance. Source: [J2].

Fig. 4.3 shows the traditional MIMO impedance calculation method without the impact of the grid impedance. Two uncorrelated PRBSs are injected on the *d*-axis and *q*-axis, respectively. Based on the cross-correlation method, the voltage responses $\triangle U_{dq1}$ and $\triangle U_{dq2}$ are distinguished from different contributions of uncorrelated signals in the frequency-domain. With the DFT, the impedance can be easily calculated as

$$Z_{dd} = \frac{\Delta U_{d1}}{\Delta I_d}\bigg|_{\Delta I_q = \mathrm{PRBS2}} \qquad Z_{qd} = \frac{\Delta U_{q1}}{\Delta I_d}\bigg|_{\Delta I_q = \mathrm{PRBS2}} \tag{4.1}$$

The entries of the impedance matrix, Z_{dq}, Z_{qq} is able to be calculated as:

$$Z_{dq} = \frac{\Delta U_{d2}}{\Delta I_q}\bigg|_{\Delta I_d = \mathrm{PRBS1}} \qquad Z_{qq} = \frac{\Delta U_{q2}}{\Delta I_q}\bigg|_{\Delta I_d = \mathrm{PRBS1}} \tag{4.2}$$

Since two uncorrelated PRBSs are adopted for simultaneously perturbing the measuring system, the MIMO impedance matrix is equivalently divided into four SISO elements for the measurement.

4.3. Impact of Grid Impedance on Traditional MIMO Impedance Calculation

It is not reasonable to assume the grid impedance is equal to zero in the practical system and its impact on traditional MIMO impedance calculation must take into account. Fig. 4.4 gives the system diagram to illustrate the impact mechanism of the grid impedance on calculated impedance when using traditional MIMO impedance calculation. Due to the presence of the grid impedance, measured *d*-axis responses are correlated with *q*-axis responses, which makes the traditional MIMO impedance calculation inaccurate.

When PRBS1 and PRBS2 are respectively injected on the *d*-axis and *q*-axis, the voltage response $\triangle U_{dq}$ cannot be distinguished from the different contributions of perturbations $\triangle I_{dq}$ due to the additional disturbance current responses $\triangle I_{gdq}$ introduced by the grid impedance. In this case, the traditional MIMO impedance calculation results can be obtained

$$\frac{\Delta U_{d1}}{\Delta I_{d1}} = Z_{dd} + Z_{dq}\frac{\Delta I_{q1}}{\Delta I_{d1}}\bigg|_{\Delta I_{q1}=-\Delta I_{gq1}} \qquad \frac{\Delta U_{q1}}{\Delta I_{d1}} = Z_{qd} + Z_{qq}\frac{\Delta I_{q1}}{\Delta I_{d1}}\bigg|_{\Delta I_{q1}=-\Delta I_{gq1}} \tag{4.3}$$

where disturbance current $\triangle I_{q1}$ is introduced by the grid admittance and can be expressed as

$$\Delta I_{q1} = -\Delta I_{gq1} = -Y_{gqd}\Delta U_{d1} - Y_{gqq}\Delta U_{q1} \tag{4.4}$$

Substituting equation (4.4) into equation (4.3), the calculated results related to the PRBS1 are derived as

$$\frac{\Delta U_{d1}}{\Delta I_{d1}} = \frac{Z_{dd} + Y_{gqq}Z_{qq}Z_{dd} - Z_{qd}Z_{dq}Y_{gqq}}{1 + Y_{gqq}Z_{qq} + Y_{gqd}Z_{dq}} \qquad \frac{\Delta U_{q1}}{\Delta I_{d1}} = \frac{Z_{qd} + Y_{gqd}Z_{dq}Z_{qd} - Z_{dd}Z_{qq}Y_{gqd}}{1 + Y_{gqq}Z_{qq} + Y_{gqd}Z_{dq}} \tag{4.5}$$

Similarly, the traditional MIMO calculation results related to PRBS2 can be expressed as

$$\frac{\Delta U_{d2}}{\Delta I_{q2}} = \frac{Z_{dq} + Y_{gdq}Z_{qd}Z_{dq} - Z_{qq}Z_{dd}Y_{gdq}}{1 + Y_{gdq}Z_{qd} + Y_{gdd}Z_{dq}} \qquad \frac{\Delta U_{q2}}{\Delta I_{q2}} = \frac{Z_{qq} + Y_{gdd}Z_{dd}Z_{qq} - Z_{dq}Z_{qd}Y_{gdd}}{1 + Y_{gdq}Z_{qd} + Y_{gdd}Z_{dq}} \tag{4.6}$$

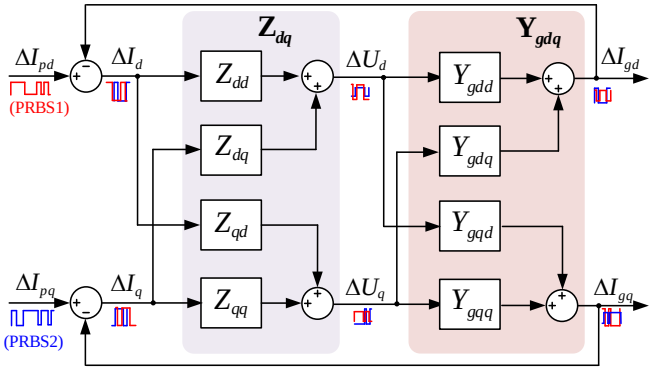

Figure 4.4. Coupling effect of the grid impedance on traditional MIMO impedance calculation. Source: [J2].

It is proved that the calculated results by using the traditional MIMO impedance calculation method, are not the actual impedance matrix and are significantly influenced by the grid admittance.

4.4. Time-Domain MIMO Parametric Impedance Identification Technique

4.4.1. Principle of MIMO Parametric Identification Method

Fig. 4.5 depicts the principle of the time-domain MIMO parametric impedance identification method. The purpose of the approach is to identify four proper transfer

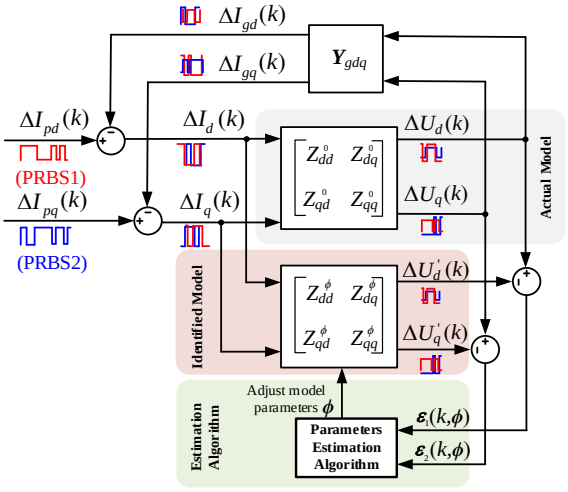

Figure 4.5. Principle of the time-domain MIMO parametric impedance identification method. Source: [J2].

functions for elements of the impedance matrix $\mathbf{Z}_{dq}^{\phi}$ on the basis of the voltage and current response in the time domain such that the identified impedance model is able to precisely represent the characteristic of the actual impedance model $\mathbf{Z}_{dq}^{0}$.

The structure of the identified transfer function is first selected and the predicted output can be expressed by

$$\Delta U_d^{'}(k) = \frac{B_{11}(z)}{A_1(z)}\Delta I_d(k) + \frac{B_{12}(z)}{A_1(z)}\Delta I_q(k) = Z_{dd}^{\phi}(z)\Delta I_d(k) + Z_{dq}^{\phi}(z)\Delta I_q(k) \quad (4.7)$$

where $Z_{dd}^{\phi}(z)$ and $Z_{dq}^{\phi}(z)$ means the transfer functions of the impedance matrix to be identified. $A_1(z)$, $B_{11}(z)$ and $B_{12}(z)$ represent the denominator and numerators of polynomials of $Z_{dd}^{\phi}(z)$ and $Z_{dq}^{\phi}(z)$, whose coefficients formulate the estimated parameters vector ϕ.

The prediction error method (PEM) is then, employed to map the relationship between the measured responses and the estimated parameters, which can be derived as

$$\varepsilon_1(k,\phi) = \Delta U_d(k) - \Delta U_d^{'}(k) = (Z_{dd}^{0} - Z_{dd}^{\phi})\Delta I_d(k) + (Z_{dq}^{0} - Z_{dq}^{\phi})\Delta I_q(k) \quad (4.8)$$

where $Z_{dd}^{0}(z)$ and $Z_{dq}^{0}(z)$ denote the real transfer functions of the impedance matrix elements. The input signals $\Delta I_d(k)$ and $\Delta I_q(k)$ for the identification are correlated with each other due to the impact of the grid impedance. It seems that their contributions to the specific voltage response cannot be distinguished. However, with PEM, the accuracy of the identified results is not affected by the correlation of input signals used for the impedance calculation. To prove the conclusion, the equivalent block of the MIMO impedance identification technique is formulated, as shown in Fig. 4.6. To ensure the prediction error to be approximately zero, Z_{dd}^{0}–Z_{dd}^{ϕ} and Z_{dq}^{0}–Z_{dq}^{ϕ} terms have to be zero such that the minimum value of equation (4.8) can be obtained. The detailed process can be found in [J3].

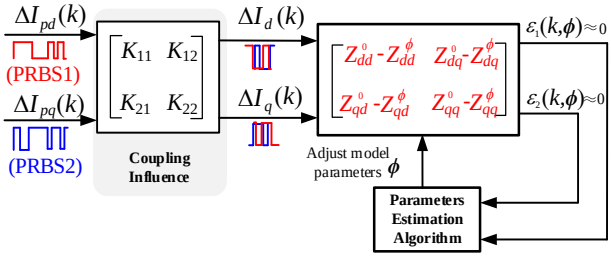

Figure 4.6. Equivalent block of MIMO impedance identification technique with the impact of grid impedance. Source: [J2].

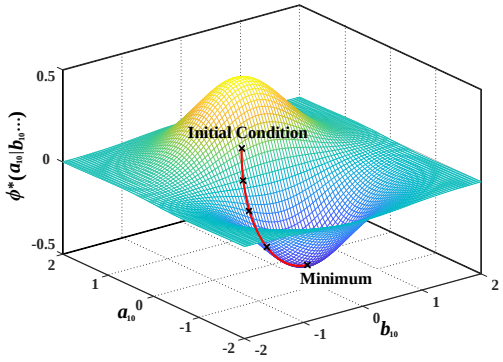

Figure 4.7. Illustration of the basic idea of the gradient descent algorithm. Source: [J2].

The least-squares method is employed to estimate the parameters of the identified model and the expression can be written as

$$\phi^* = \arg\min_{\phi} \frac{1}{N}\sum_{k=1}^{N}[\varepsilon_1(k,\phi)]^2 \tag{4.9}$$

where "arg min" means the minimum value of the expression. The gradient descent method is further employed to obtain this minimum value and the specific expression can be derived as:

$$\psi(k,\phi) \triangleq -\frac{\partial Z_{dd}^{\phi}}{\partial \phi}\Delta I_d(k) - \frac{\partial Z_{dq}^{\phi}}{\partial \phi}\Delta I_q(k) \tag{4.10}$$

Fig. 4.7 gives an example for the illustration of the basic idea of the gradient descent algorithm, where identified parameters are continuously tuned in the opposite direction of the gradient of $\psi(k,\phi)$ such that the minimum value can be obtained.

4.4.2. Implementation of Time-Domain MIMO Impedance Identification Method

Fig. 4.8 illustrated the implementation procedure of MIMO parametric identification for VSC impedance measurement. It is mainly composed of four parts. A detailed explanation of each part can be found in [J1]. The System Identification Toolbox of MATLAB is applied to achieve parametric identification. The details can be found in [J3].

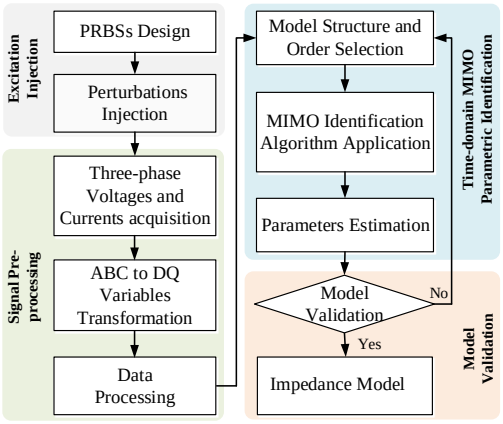

Figure 4.8. The procedure of timed-domain MIMO parametric identification for VSC impedance measurement. Source: [J2].

4.5. Experiment Validation

To verify the effectiveness of the proposed time-domain MIMO parametric identification method, a prototype of the impedance measurement unit is established, as shown in Fig. 4.9.

Based on the experiment data, the numerical expression of the *z*-domain transfer function of the admittance model can be identified as:

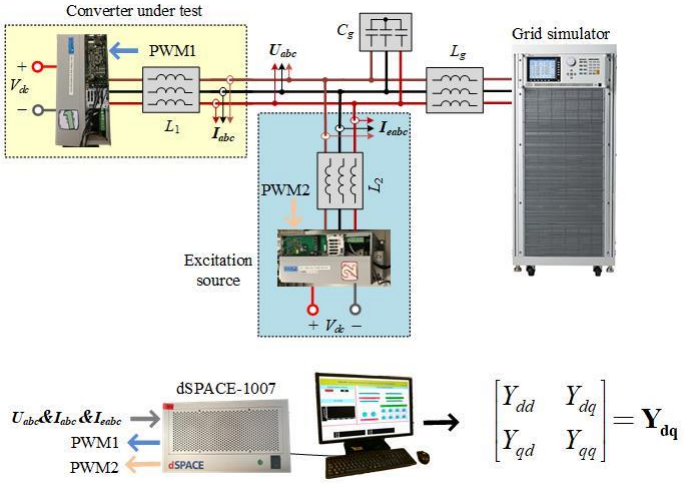

Figure 4.9. The prototype of the impedance measurement unit. Source: [J2].

$$Y_{dd} = \frac{0.006 - 0.065z^{-1} - 0.07z^{-2} + 0.07z^{-3} + 0.065z^{-4} - 0.005z^{-5}}{1 + 1.1z^{-1} - 1.4z^{-2} - 1.6z^{-3} + 0.4z^{-4} + 0.5z^{-5}}$$

$$Y_{dq} = \frac{-0.008z^{-1} + 0.006z^{-2} - 0.004z^{-3} + 0.004z^{-4} + 0.009z^{-5}}{1 - 0.71z^{-1} - 1.29z^{-2} + 0.23z^{-3} + 0.81z^{-4} + 0.41z^{-5}}$$

$$Y_{qd} = \frac{0.002 - 0.008z^{-1} + 0.026z^{-2} + 0.008z^{-3} - 0.028z^{-4}}{1 - 0.84z^{-1} - 0.84z^{-2} + 0.84z^{-3} - 0.16z^{-4}}$$

$$Y_{qq} = \frac{0.0005 + 0.073z^{-1} + 0.19z^{-2} - 0.21z^{-3} + 0.13z^{-4} - 0.04z^{-5}}{1 - 2.08z^{-1} + 1.08z^{-2} - 0.09z^{-3} + 0.26z^{-4} - 0.17z^{-5}}$$

Fig. 4.10-4.13 illustrates the frequency response results of the admittance model of Y_{dd}, Y_{dq}, Y_{qd} and Y_{qq}. The theoretical admittance model of VSC is calculated for the validation of the accuracy of the identified admittance model. The measured frequency range of admittance models is 1 Hz -1000 Hz. It is proved that the time-domain MIMO parametric impedance identification method can yield precise measurement results that match well with the theoretical model.

To further validate the accuracy of the identified model, the current responses of the theoretical model and identified model are compared on the basis of the same excitation inputs, as shown in Fig. 4.10 and Fig. 4.11. The compared results illustrate that the fitting ratios between the theoretical admittance model and the identified admittance model are 90.93% and 87.58%, respectively, indicating the effectiveness of the proposed identification method for mitigation of the impact of the grid impedance.

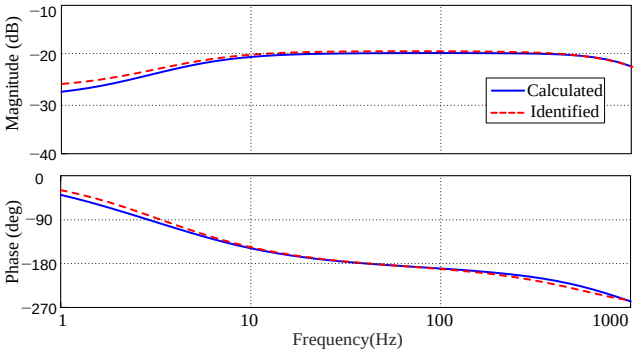

Figure 4.10. Comparison between theoretical admittance model and identified admittance model of Y_{dd}. Source: [J2].

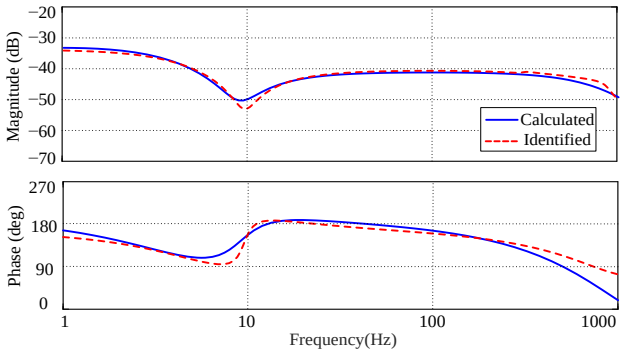

Figure 4.11. Comparison between theoretical admittance model and identified admittance model of Y_{dq}. Source: [J2].

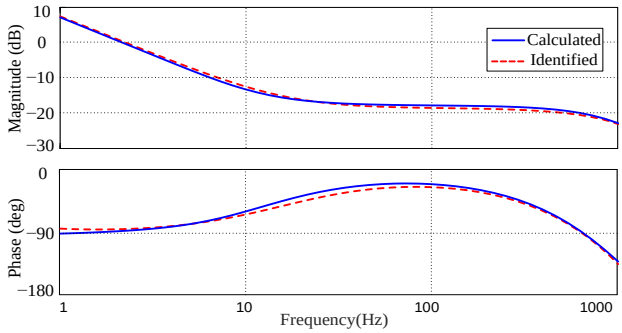

Figure 4.12. Comparison between theoretical admittance model and identified admittance model of Y_{qd}. Source: [J2].

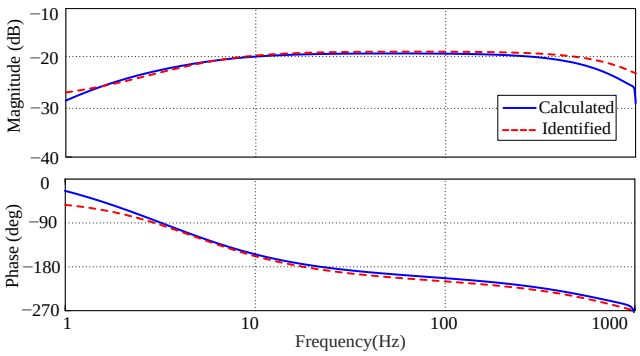

Figure 4.13. Comparison between theoretical admittance model and identified admittance model of Y_{qq}. Source: [J2].

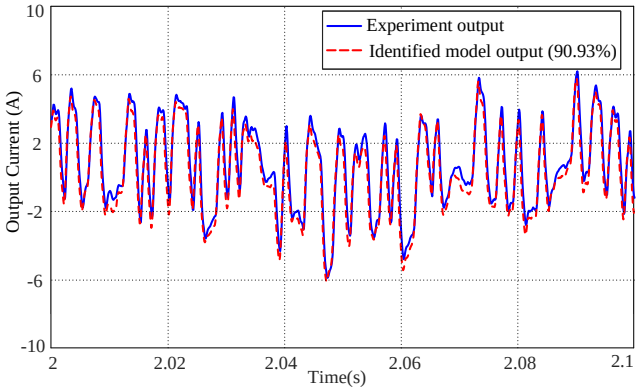

Figure 4.14. Comparison for output responses of *d*-axis current between the theoretical model and identified model. Source: [J2].

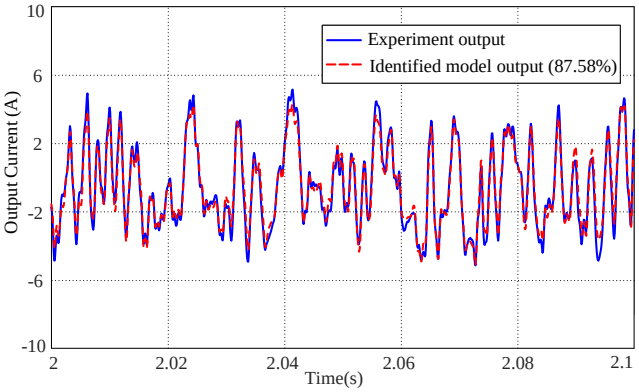

Figure 4.15. Comparison for output responses of *q*-axis current between the theoretical model and identified model. Source: [J2].

More detailed discussions and case studies can be found in [J2] and [C3].

4.6. Summary

This chapter has revealed that the traditional MIMO impedance calculation method may yield an inaccurate VSC impedance model due to the coupling impact of the grid impedance. To avoid such an impact and effectively measure the impedance matrix, a time-domain MIMO parametric impedance identification method is developed. Compared with the traditional MIMO impedance calculation method, the approach simultaneously applies PRBSs to directly identify the analytical model from the time-domain data, which lowers the measurement efforts and improves the accuracy of the impedance measurement.

Chapter 5. Estimation of DQ-Frame Impedance Models at Different Operating Points

The content of this chapter is based on **J**3

5.1. Introduction

This chapter develops an admittance, i.e., the inverse of impedance estimation method for VSCs at different operating points. The operating point dependence of *dq*-frame admittance is first presented through 3-D plots of frequency response. The principle and implementation procedure for admittance estimation at different operating points is then elaborated. To select the appropriate operating point interval for measurement, the estimated error is then evaluated based on the posterior error estimation method. Based on the estimation error, the criterion for the selection of operating point intervals is proposed. Lastly, the simulation results are given for the validation of the developed admittance estimation method.

5.2. Operating Point Dependence of DQ-Frame Admittance

The *dq*-frame voltages and currents are exactly the operating points determining the impedance model of VSCs. Table 5.1 shows the change range of operating points that are initially defined in the work. The range can be selected based on the user's interest and the power rating of the converter. For simplicity, the variation of *d*-axis voltage and current is only considered and the *q*-axis is kept constant, yet it is easily extended.

Fig. 5.1 shows the variation of the *dq*-frame admittance at the specific frequency (5 Hz) under different sets of *d*-axis voltage and current. It is concluded that the admittance model of VSC is highly dependent on the operating point due to the dynamics of the outer power control and synchronization control. Consequently, the VSC admittance cannot be only measured at one specific operating point.

Table 5.1. Operating Points of VSC. Source: [J3].

Variables	Variation range
d-axis voltage (U_d)	100 V ~ 400 V
d-axis current (I_d)	0 A ~ 20 A
q-axis current (I_q)	5 A

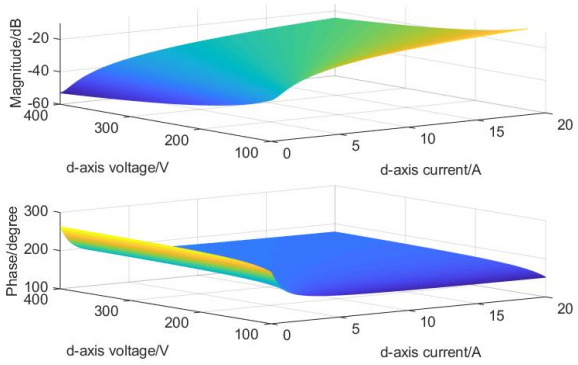
Magnitude/dB
-20
-40
-60
400
300
200
100
d-axis voltage/V
0
5
10
15
20
d-axis current/A
Phase/degree
300
200
100
400
300
200
100
d-axis voltage/V
0
5
10
15
20
d-axis current/A

(a)

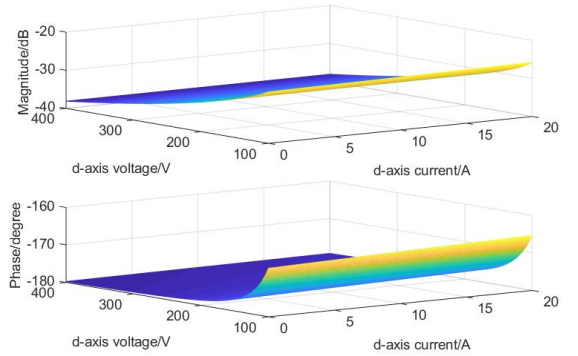
Magnitude/dB
-20
-30
-40
400
300
200
100
d-axis voltage/V
0
5
10
15
20
d-axis current/A
Phase/degree
-160
-170
-180
400
300
200
100
d-axis voltage/V
0
5
10
15
20
d-axis current/A

(b)

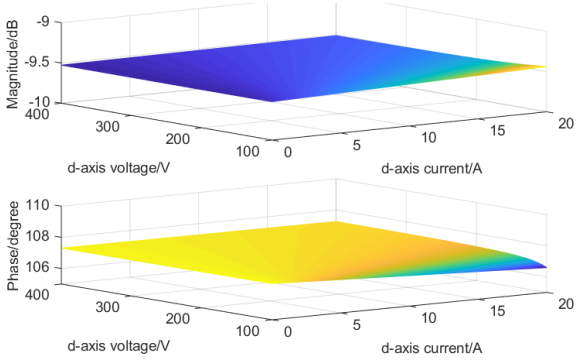
Magnitude/dB
-9
-9.5
-10
400
300
200
100
d-axis voltage/V
0
5
10
15
20
d-axis current/A
Phase/degree
110
108
106
400
300
200
100
d-axis voltage/V
0
5
10
15
20
d-axis current/A

(c)

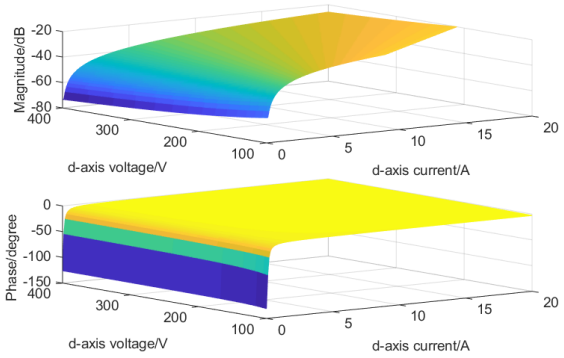

(d)

Figure 5.1. Variation of the *dq*-frame admittance at 5 Hz with different sets of *d*-axis voltage and current. (a) Y_{dd}. (b) Y_{dq}. (c) Y_{qd}. (d) Y_{qq}. Source: [J3].

5.3. Admittance Estimation at Different Operating Points

Fig. 5.2 shows the detailed procedure of the admittance estimation method of VSCs covering different operating points. It mainly consists of three parts: lookup-tables formulation, the admittance estimation, and the operating point interval adjustment.

The lookup-tables are used for storing the measured admittance results at a defined set of operating points. When the intervals of measured operating points are chosen again, the lookup-tables will be updated correspondingly. Since the admittance matrix contains four entries i.e. Y_{dd}, Y_{dq}, Y_{qd} and Y_{qq}, four lookup-tables are, therefore, required to store the measured results.

Fig. 5.3 shows the principle of the admittance estimation for VSCs under different operating points at one specific frequency point. Based on the measured admittance results stored in lookup-tables, a piecewise linear function Y_e is obtained such that it can approximately descript the real admittance Y. Thus, the interpolation method is adopted.

Fig. 5.4 (a) illustrates the geometric representation of bilinear interpolation. Given the measured admittance results: Y_{11}=(V_{d1}, I_{d1}), Y_{12}=(V_{d1}, I_{d2}), Y_{21}=(V_{d2}, I_{d1}), and Y_{22}=(V_{d2}, I_{d2}), it formulates an admittance plane. To estimate the admittance at the unmeasured operating point (V_d, I_d), the two-dimensional (bilinear) interpolation is implemented using linear interpolation first in one direction, and then again in the other direction.

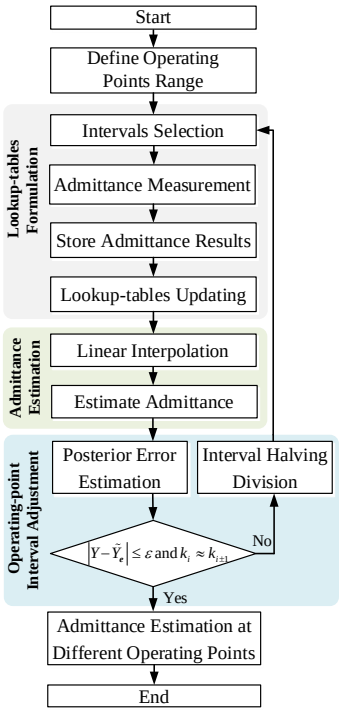

Figure 5.2. The procedure of the admittance estimation method at different operating points. Source: [J3].

The linear interpolation is first implemented in the V_d-direction. This yields: (blue dots, as shown in Fig. 5.4)

$$Y(V_d, I_{d1}) = \frac{V_{d2} - V_d}{V_{d2} - V_{d1}} Y_{11} + \frac{V_d - V_{d1}}{V_{d2} - V_{d1}} Y_{21} \quad Y(V_d, I_{d2}) = \frac{V_{d2} - V_d}{V_{d2} - V_{d1}} Y_{12} + \frac{V_d - V_{d1}}{V_{d2} - V_{d1}} Y_{22} \quad (5.1)$$

Second, based on interpolated points, as shown in (5.1), the linear interpolation is further processed in the I_d-direction to obtain the estimated admittance: (black dot, as shown in Fig. 5.4)

$$Y(V_d, I_d) = \frac{I_{d2} - I_d}{I_{d2} - I_{d1}} Y(V_d, I_{d1}) + \frac{I_d - I_{d1}}{I_{d2} - I_{d1}} Y(V_d, I_{d2}) \quad (5.2)$$

The admittance at the unmeasured operating points can be thus estimated by using the linear interpolation method in two directions, respectively. Yet, it is more practical to consider three variables, e.g. *d*-axis voltage and *dq*-axis currents. The three-dimensional (trilinear) interpolation method is therefore used for the estimation of the admittance models.

Fig. 5.4 (b) illustrates the geometric representation of trilinear interpolation. It is usually performed by using the linear interpolation first in one direction (obtaining blue dots), and then again in another direction (obtaining green dots), and in the last direction (obtaining black dots). Since the principle of the trilinear interpolation is the same as the bilinear interpolation, the detailed derivation will be neglected for simplicity.

Fig. 5.5 illustrates the variation of the estimated admittance plane for Y_{dd} at a single frequency point (5 Hz) with different sets of operating points. The lookup-table is first formulated based on 15 measured data points. Based on the bilinear interpolation method, the converter admittance model is estimated by using a group of 4 measured data points stored in the lookup-table. The estimated admittance plane is consists of 8 admittance sub-planes, as can be seen from the green plane in Fig. 5.5.

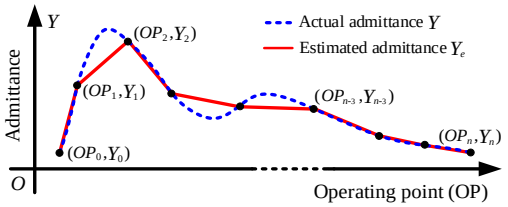

Figure 5.3. Principle for admittance estimation under different operating points at one specific frequency point. Source: [J3].

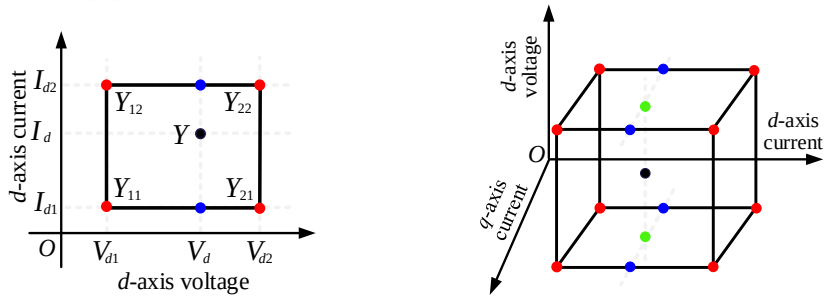

Figure 5.4. Geometric representation. (a) Bilinear interpolation. (b) Trilinear interpolation. Source: [J3].

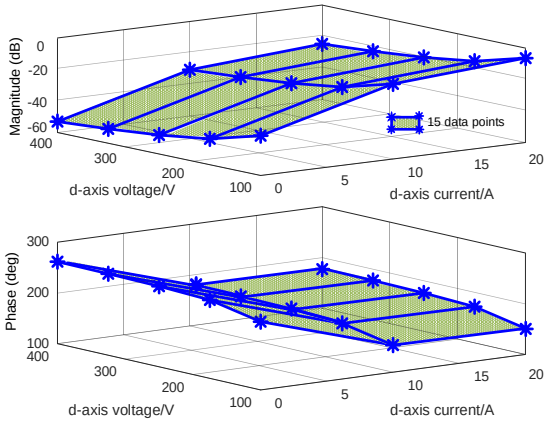

Figure 5.5. Variation of the estimated admittance for Y_{dd} at 5 Hz with different sets of operating points. Source: [J3].

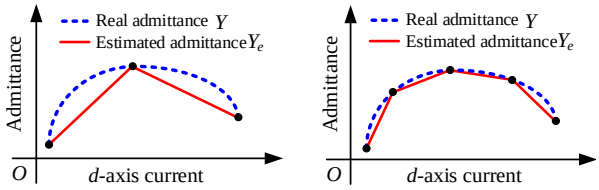

Figure 5.6. Comparison between the real admittance and estimated admittance by using different operating point intervals. Source: [J3].

5.4. Operating Points Intervals Adjustment for Admittance Measurement

Fig. 5.6 shows the comparison between the real admittance model and the estimated admittance model by using different operating point intervals. The accuracy of the estimated admittance model is dependent on the number of measured data points. It is clear that the estimated admittance model will more accurate if more data points are used. Consequently, more measurement time is required, and the efficiency of the admittance measurement is further reduced. There is thus a trade-off between measurement accuracy and efficiency. To manage them holistically, the appropriate intervals for the measured operating points should be selected accordingly based on the relationship between the estimation error and the number of measured data points.

5.4.1. Error Estimation of Estimated Admittance Model

The estimation errors are derived based on the estimated admittance results in two directions [66], [67], respectively. Starting from the V_d-direction, the estimation error R_{ev} between the real admittance Y and estimated admittance Y_{ev} can be expressed as

$$R_{ev} = Y - Y_{ev} \approx \frac{\partial Y^{''}(V_d, \tau_2)}{\partial I_d^2}(I_d - I_{d1})(I_d - I_{d2}) + \frac{\partial Y^{''}(\tau_1, I_d)}{\partial V_d^2}(V_d - V_{d1})(V_d - V_{d2}) \tag{5.3}$$

where $\partial Y^{''}$ represents the second-order partial derivative of real admittance Y. τ_1 and τ_2 means the arbitrary values within measured operating points ($V_{d1,2}$ and $I_{d1,2}$). Since the real admittance is unknown, equation (5.3) cannot be used for error estimation directly. The posterior error estimation method is thus employed to obtain the estimation error.

Given another measured data point (V_{d3}, Y_3) with the range of [V_{d1}, V_{d2}], the estimation error can be derived as:

$$\tilde{R}_{ev} = Y - \tilde{Y}_{ev} - \frac{\partial Y^{''}(V_d, \tau_2)}{\partial I_d^2}(I_{di} - I_{d1})(I_{di} - I_{d2}) \approx \frac{\partial Y^{''}(\tau_3, I_{di})}{\partial V_d^2}(V_d - V_{d1})(V_d - V_{d3}) \tag{5.4}$$

Since $\partial Y^{''}$ is approximately constant with the range of [V_{d1}, V_{d3}], the estimation error in the V_d-direction $\tilde{R}_{ev}$ is calculated based on (5.3) and (5.4), which can be written as

$$\tilde{R}_{ev} = Y - \tilde{Y}_{ev} \approx \frac{V_d - V_{d3}}{V_d - V_{d2}}(\tilde{Y}_{ev} - Y_{ev}) \tag{5.5}$$

Similarly, the estimation error in the I_d-direction can be calculated as

$$\tilde{R}_e = Y - \tilde{Y}_e \approx \frac{I_d - I_{d3}}{I_d - I_{d2}}(\tilde{Y}_e - Y_e) \tag{5.6}$$

5.4.2. Adjustment Criteria of Operating Point Intervals

To choose proper intervals of operating points in two-dimensional, the estimation error is ensured to satisfy the accuracy requirement first in the V_d-direction and the estimation error in the I_d-direction is next guaranteed to meet the requirements.

The interval of the *d*-axis voltage is first selected. Givens that V_{di} (i=0,1,..,n) is a group of n_1+1 points which satisfied $a \leq V_{d0} < V_{d1} < V_{d2} < \ldots. V_{dn} \leq b$ and distributed on the defined range of operating point [a, b] equidistantly, then operating-point interval h_1 can be obtained as

$$h_1 = (b-a)/n_1, \quad V_{di} = V_{d0} + i\,h_1 \tag{5.7}$$

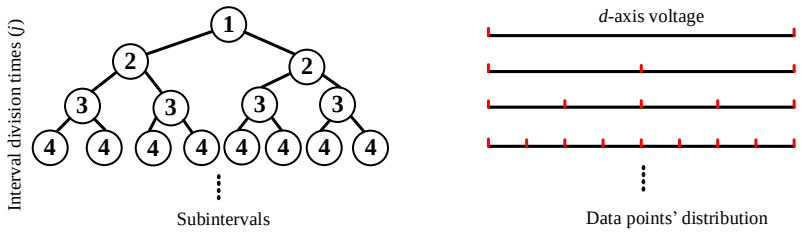

(a) (b)

Figure 5.7. The binary tree structure for interval selection of operating point. (a) The number of subintervals and division times of interval. (b) Operating points' distribution. Source: [J3].

If the operating-point interval h_1 is halved, there are $2n_1+1$ equidistant data points distributed on the interval $[a, b]$. Based on (5.5) and (5.7), the maximum estimation error at each subinterval can be derived when V_d is located at the midpoint of subinterval $[V_{di}, (V_{di}+V_{di+1})/2]$. Thus,

$$\tilde{R}_{evm} = Y - \tilde{Y}_{ev} \approx \frac{1}{3}(\tilde{Y}_{ev} - Y_{ev}) \approx \frac{h_1^2}{32}\frac{\partial Y''(\varsigma_1, I_{di})}{\partial V_d^2}, V_{di} < \varsigma_1 < \frac{V_{di}+V_{di+1}}{2} \tag{5.8}$$

If the deviation of the two estimated admittance results at all subinterval meets:

$$\frac{1}{3}\left|\tilde{Y}_{ev} - Y_{ev}\right| \le \varepsilon \tag{5.9}$$

then $\left|Y - \tilde{Y}_{ev}\right| \le \varepsilon$, that is to say, the admittance of $\tilde{Y}_{ev}$ estimated by using $2n_1+1$ data points in the V_d-direction meets the accuracy requirements.

On the other hand, if the estimation error is not satisfied with the error-index requirement, the operating-point interval is halved and more data points need to be measured. With (5.8) and (5.9), an iterative process of the interval selection of operating point can be constructed, as shown in Fig. 5.2, where the intervals will be adjusted constantly until the accuracy requirements are met.

Fig. 5.7 shows the interval selection of the operating point with the binary tree structure [68], where the numbers mean interval division times in Fig. 5.8 (a) and data points distribution is illustrated in Fig. 5.8 (b).

5.5. Simulation Validation

To verify the effectiveness of the admittance estimation method and the accuracy of the proposed interval selection criteria, an admittance measurement unit is simulated. Table 5.2 illustrates the required number of measured data points for Y_{dd} with different error indexes.

Fig. 5.8 illustrates the compared results of Y_{dd} at 5 Hz with different error indexes of 1% (green plan) and 10% (red plan). Only intervals of *d*-axis voltage and current are given for simplicity. It can be seen from the figure that a smaller error-index results in more measured data points.

The admittance at the operating points U_{d0}=225 V, I_{d0}=5 A, I_{q0}=5 A, is estimated by using different error-indexes. Fig. 5.9 gives the comparison results between the theoretical admittance and estimated admittance of Y_{dd} with different error indexes. With a smaller error-index, the estimated admittance tends to be more accurate, yet the required number of measured data points is increased. If the admittance is estimated in multi-dimensional, the measurement process is time-consuming and

Table 5.2. Required Number of Measured Data Points for Y_{dd}. Source: [J3].

Error Index (≤)	Number of interval division times *j*	Number of data points
1%	U_d: 3 I_d:2 I_q:2	5×3×3=45
5%	U_d: 2 I_d:1 I_q:1	3×2×2=12
10%	U_d: 1 I_d:1 I_q:1	2×2×2=8

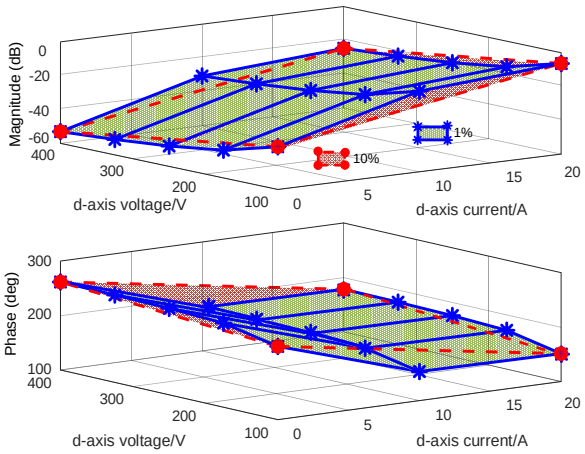

Figure 5.8. Compared results of Y_{dd} at 5 Hz with different error indexes. Source: [J3].

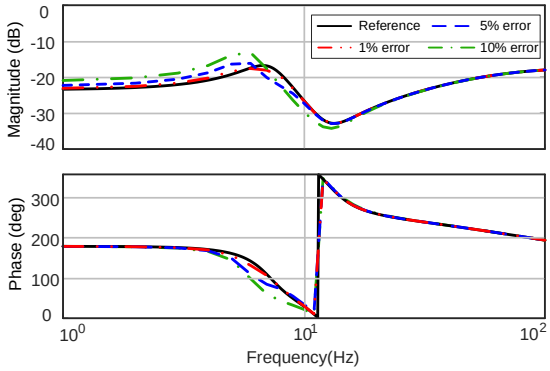

Figure 5.9. Comparison between theoretical admittance and estimated admittance of Y_{dd} with different error indexes. Source: [J3].

inefficient. On the contrary, the larger the error-index would cause the more inaccurate the estimated admittances. Consequently, there is a trade-off between the efficiency of the measurement and the accuracy of the estimated admittance. On the other hand, in the higher frequency range (above 50 Hz), operating points have no impact on the admittance shaping. With different error-indexes, the same admittance results can be estimated.

Table 5.3 illustrates the required number of measured data points for Y_{dq} with different error indexes. Fig. 5.10 illustrates the comparison between the theoretical admittance and estimated admittance of Y_{dq}. It can be seen from the figure that fewer numbers of measured data points are required compared with the estimation of Y_{dd}. This is due to the fact that the operating point dependence of this term is mainly caused by PLL. Thus, the nonlinear effect is dominated by the *d*-axis voltage and *q*-axis current, which should have more intervals for accurate admittance estimation.

Table 5.3. Required Number of Measured Data Points for Y_{dq}. Source: [J3].

Error Index (≤)	Number of interval division times *j*	Number of data points
1%	U_d: 3 I_d:1 I_q:2	5×2×3=30
5%	U_d: 2 I_d:1 I_q:1	3×2×2=12
10%	U_d: 1 I_d:1 I_q:1	2×2×2=8

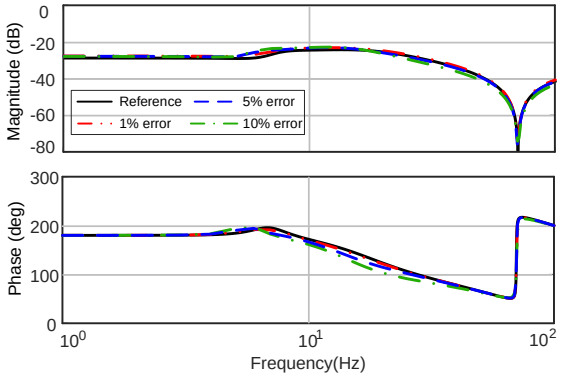

Figure 5.10. Comparison between theoretical admittance and estimated admittance of Y_{dq} with different error indexes. Source: [J3].

Table 5.4 gives the required number of measured data points for Y_{qd}. Fig.5.11 illustrates the comparison between the theoretical admittance and estimated admittance of Y_{qd}. The same intervals of operating pints are calculated with different error indexes. This is because that the admittance term of Y_{qd} is linear and not dependent on the operating points. Thus, the initial interval of operating points is employed to accurately estimate the admittance of Y_{qd}.

Table 5.4. Required Number of Measured Data Points for Y_{qd}. Source: [J3].

Error Index (≤)	Number of interval division times j	Number of data points
1%	U_d: 1 I_d:1 I_q:1	2×2×2=8
5%	U_d: 1 I_d:1 I_q:1	2×2×2=8
10%	U_d: 1 I_d:1 I_q:1	2×2×2=8

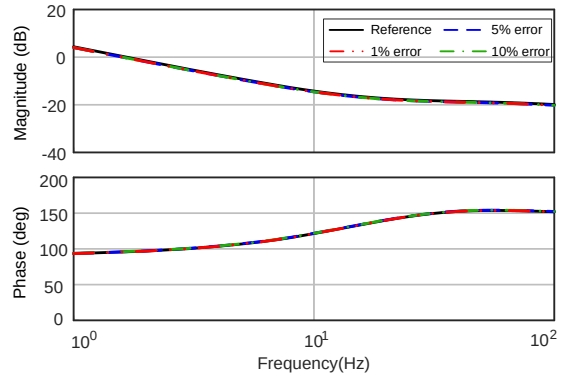

Figure 5.11. Comparison between theoretical admittance and estimated admittance of Y_{qd} with different error indexes. Source: [J3].

Table 5.5. Required Number of Measured Data Points for Y_{qq}. Source: [J3].

Error Index (≤)	Number of interval division times *j*	Number of data points
1%	U_d: 3 I_d:2 I_q:1	5×3×2=30
5%	U_d: 2 I_d:1 I_q:1	3×2×2=12
10%	U_d: 1 I_d:1 I_q:1	2×2×2=8

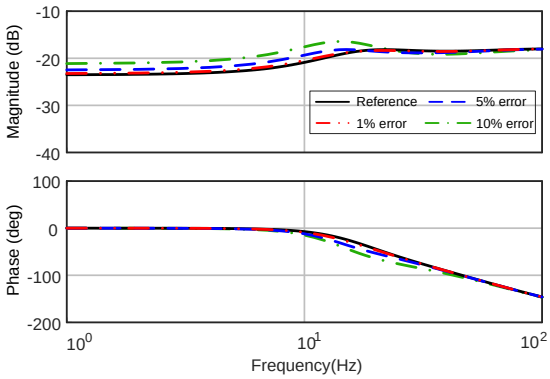

Figure 5.12. Comparison between theoretical admittance and estimated admittance of Y_{qq} with different error indexes. Source: [J3].

Table 5.5 illustrates the required number of measured data points for Y_{qq}. Fig. 5.12 shows the comparison between the theoretical admittance and estimated admittance of Y_{qq}. Due to the nonlinear effect of PLL, a smaller error-index tend to increase the number of interval division times of *d*-axis voltage and current, which can obtain more accurate estimated admittance.

More detailed discussions and case studies can be found in [J3].

5.6. Summary

This chapter has proposed a *dq*-frame admittance estimation method covering different operating points. In the approach, the frequency-domain measured results are first stored in the lookup-tables, and the multi-dimensional interpolation method is then employed to estimate converter admittances at the unmeasured operating points. To evaluate the accuracy of the estimated admittance models, the posterior error estimation method is adopted, from which a selection criterion has also been proposed to iteratively adjust the operating-point intervals, which provides the guidance for the determination of the measured data and improves the accuracy, reliability, and efficiency of the admittance measurement.

Chapter 6. Conclusions

6.1. Conclusions

This Ph.D. project has developed several methods to accurately and efficiently measure the *dq*-frame impedance model of three-phase VSCs. An impedance estimation method of VSCs covering a wide range of operating points is further proposed. The main findings of the Ph.D. thesis are listed as follows:

- This project proposes a systematic method for designing perturbation signals. In the approach, four performance indexes are defined to evaluate the quality of different types of perturbation signals, revealing that the selection of the perturbation signal is a compromise between these performance indexes. To avoid the frequency coupling effect of nonlinear control dynamics of VSCs, the frequency components of the selected perturbation signal are intentionally determined.

- The impact of *dq*-transformation on the impedance measurement has been investigated in this project. It is found that the synchronization dynamics caused by PLL and grid fundamental frequency variation have significant impacts on the accuracy of the *dq*-frame impedance measurement results. An improved PLL is thus proposed to avoid the negative effect.

- The impact of the grid impedance on the impedance measurement has also been analyzed in detail. It is revealed that the grid impedance leads to a coupling effect on the traditional MIMO impedance calculation, which adversely affect the accuracy of impedance measurement. To avoid the adverse effects, this project proposes a time-domain MIMO parametric identification method to directly calculate the impedance matrix of VSCs, which simultaneously improves the accuracy and efficiency of impedance measurement.

- This project has proposed a technique that can estimate the *dq*-frame impedance models of VSCs over a wide range of operating points. In the approach, the multi-dimensional interpolation method is employed to estimate the unmeasured impedance models with a limited set of measured data, and the posterior error estimation method is introduced to evaluate the estimation error. Based on the estimated error, the needed set of measurement data for impedance estimation can be determined.

6.2. Future Work

There are still some open questions which have not been addressed in this Ph.D. project and are worth to investigating in the future.

- This project only considers the impedance measurement of VSCs in the *dq*-frame. It is, therefore, encouraging to develop an impedance measurement method of VSCs in the stationary ($\alpha\beta$-) frame, and the factors that influence the accuracy of this measurement is worth investigating in future research.

- The selection of the perturbation signal magnitude has not been discussed in the project, which should provide clear guidance in future research such that the high SNR can be achieved and simultaneously nonlinear responses are not excited.

- The accuracy of the measured impedance model is validated through the theoretical model of VSC in this project. However, the analytical model itself might not be accurate, which motivates us to find a more convincing method for model validation.

- There are many kinds of parametric identification methods which owe different advantages and disadvantages. However, this project only uses the prediction error based MIMO parametric identification method for the impedance measurement. Thus, it is interesting to investigate different algorithms for impedance measurement.

- In this Ph.D. project, the impedance estimation method is only based on linear interpolation techniques. It would be interesting to exploit artificial intelligent techniques, e.g. machine learning and deep learning algorithms for the impedance estimation covering multiple operating points.

- This project is focused on how to obtain the accurate *dq*-frame impedance model of VSC. Yet, the system-level application of the measured impedance model for stability analysis and identification of root causes of instability still requires more research effort.

Bibliography

[1] B. Kroposki, B. Johnson, "Achieving a 100% renewable grid: operating electric power systems with extremely high levels of variable renewable energy," *IEEE Power and Energy Magazine*, vol. 15, no. 2, pp. 61-73, March-April 2017.

[2] N. Flourentzou, V. G. Agelidis and G. D. Demetriades, "VSC-based HVDC power transmission systems: an overview," *IEEE Trans. Power Electron.*, vol. 24, no. 3, pp. 592-602, March 2009.

[3] A. de la Villa Jaen, E. Acha and A. G. Exposito, "Voltage source converter modeling for power system state estimation: STATCOM and VSC-HVDC," *IEEE Trans. Power Systems*, vol. 23, no. 4, pp. 1552-1559, Nov. 2008.

[4] F. Blaabjerg, Z. Chen, and S. B. Kjaer, "Power electronics as efficient interface in dispersed power generation systems," *IEEE Trans. Power Electron.*, vol. 19, no. 5, pp. 1184-1194, Sep. 2004.

[5] B. Ferreira, "Understanding the challenges of converter networks and systems: Better opportunities in the future," *IEEE Power Electron. Mag*., vol. 3, no. 2, pp. 46–49, Jun. 2016.

[6] X. Wang and F. Blaabjerg, "Harmonic stability in power electronic-based power systems: concept, modeling, and analysis*," IEEE Trans. Smart Grid*, vol. 10, no. 3, pp. 2858-2870, May 2019.

[7] R. D. Middlebrook, "Input filter considerations in design and application of switching regulators," in *Proc. IEEE Ind. Appl. Soc. Conf*., Oct. 1976, pp. 94–107.

[8] M. Belkhayat, "Stability criteria for ac power systems with regulated loads," Ph.D. dissertation, Purdue Univ., West Lafayette, IN, USA, Dec. 1997.

[9] R. Turner, S. Walton, and R. Duke, "A case study on the application of the Nyquist stability criterion as applied to interconnected loads and sources on grids," *IEEE Trans. Ind. Electron*., vol. 60, no. 7, pp. 2740–2749, Jul. 2013.

[10] N. Bottrell, M. Prodanovic, and T. C. Green, "Dynamic Stability of a microgrid with an active load," *IEEE Trans. Power Electron*., vol. 28, no. 11, pp. 5107–5119, Nov. 2013.

[11] W. Cao, Y. Ma, L. Yang, F. Wang and L. M. Tolbert, "D–Q impedance-based stability analysis and parameter design of three-phase inverter-based AC power

systems," *IEEE Trans. Ind. Electron.,* vol. 64, no. 7, pp. 6017-6028, July. 2017.

[12] X. Wang, F. Blaabjerg and W. Wu, "Modeling and analysis of harmonic stability in an AC power-electronics-based power system," *IEEE Trans. Power Electron*., vol. 29, no. 12, pp. 6421-6432, Dec. 2014.

[13] L. Harnefors, M. Bongiorno and S. Lundberg, "Input-admittance calculation and shaping for controlled voltage-source converters," *IEEE Trans. Ind. Electron*., vol. 54, no. 6, pp. 3323-3334, Dec. 2007.

[14] B. Wen, D. Dong, D. Boroyevich, R. Burgos, P. Mattavelli and Z. Shen, "Impedance-based analysis of grid-synchronization stability for three-phase paralleled converters," *IEEE Trans. Power Electron*., vol. 31, no. 1, pp. 26-38, Jan. 2016.

[15] X. Wang, L. Harnefors, and F. Blaabjerg, "Unified impedance model of grid-connected voltage-source converters," *IEEE Trans. Power Electron.*, vol. 33, no. 2, pp. 1775–1787, Feb. 2018.

[16] A. S. Morched and P. Kundur, "Identification and modelling of load characteristics at high frequencies," *IEEE Trans. Power Systems*, vol. 2, no. 1, pp. 153-159, Feb. 1987.

[17] D. Borkowski, A. Wetula and A. Bień, "New method for noninvasive measurement of utility harmonic impedance," in *Proc 2012 IEEE Power and Energy Society General Meeting*, San Diego, CA, 2012, pp. 1-8.

[18] M. Nagpal, W. Xu and J. Sawada, "Harmonic impedance measurement using three-phase transients," *IEEE Trans. Power Delivery*, vol. 13, no. 1, pp. 272-277, Jan. 1998.

[19] J. Hui, W. Freitas, J. C. M. Vieira, H. Yang and Y. Liu, "Utility harmonic impedance measurement based on data selection," *IEEE Trans. Power Delivery*, vol. 27, no. 4, pp. 2193-2202, Oct. 2012.

[20] G. D. Breuer, J.H.Chow, T.J.Gentile, C.B.Lindh, G.Addis., "HVDC-AC harmonic interaction Part II -AC system harmonic model with comparison of calculated and measured data," *IEEE Trans. Power App. Sys.*, vol. PAS-101, no. 3, pp. 709-718, March 1982.

[21] C. Xie, S. B. Tennakoon, R. Langella, D. Gallo, A. Testa and A. Wixon, "Harmonic impedance measurement of 25 kV single phase AC supply systems," in *Proc International Conference on Harmonics and Quality of Power. Proceedings*, Orlando, FL, USA, 2000, pp. 214-219 vol.1.

[22] K. R. Godfrey, H. A. Barker and A. J. Tucker, "Comparison of perturbation signals for linear system identification in the frequency domain," *IEEE Proceedings - Control Theory and Applications*, vol. 146, no. 6, pp. 535-548, Nov. 1999.

[23] Williams, Michael Lamar, "Method for measuring stability margin at a node of a polyphase power grid," U.S. Patent 7508224.

[24] G. Francis, R. Burgos, D. Boroyevich, F. Wang, and K. Karimi, "An algorithm and implementation system for measuring impedance in the D-Q domain," in *Energy Conversion Congress and Exposition (ECCE)*, 2011 IEEE, 2011, pp. 3221–3228.

[25] M. L. Gasperi, "AC power line impedance monitoring method and system," U.S. Patent 716427516-Jan-2007.

[26] V. Valdivia, A. Lázaro, A. Barrado, P. Zumel, and C. Fernández, "Impedance identification method of three-phase balanced voltage source inverters based on load current steps," in *Proc Control and Modeling for Power Electronics (COMPEL)*, 2010 IEEE 12th Workshop on, 2010, pp. 1–7.

[27] J. Huang, K. A. Corzine and M. Belkhayat, "Small-signal impedance measurement of power-electronics-based AC power systems using line-to-line current injection," *IEEE Trans. Power Electron.*, vol. 24, no. 2, pp. 445-455, Feb. 2009.

[28] T. Roinila, T. Messo, R. Luhtala. R. Scharrenberg, E. Jong, A. Fabian, Y. Sun, "Hardware-in-the-loop methods for real-time frequency-response measurements of on-board power distribution systems," *IEEE Trans. Ind. Electron.*, vol. 66, no. 7, pp. 5769-5777, July 2019.

[29] T. Roinila, H. Abdollahi and E. Santi, "Frequency-domain identification based on pseudorandom sequences in analysis and control of DC power distribution systems: A review," *IEEE Trans. Power Electron*. vol. 36, no. 4, pp. 3744-3756, April 2021.

[30] T. Roinila, M. Vilkko and J. Sun, "Online grid impedance measurement using discrete-interval binary sequence injection," *IEEE J. Emerg. Sel. Top. Power Electron*. vol. 2, no. 4, pp. 985-993, Dec. 2014.

[31] P. Zhong, J. Sun, Z. Tian, M. Huang, P. Yu and X. Zha, "An improved impedance measurement method for grid-connected inverter systems considering the background harmonics and frequency deviation," *IEEE J. Emerg. Sel. Top. Power Electron*, early access, 2020.

[32] B. Zhou, M. Jacsic. “Small-signal impedance identification of three phase diode rectifier with multi-frequency injection”, in *Proc. Appl. Power Electron. Conf. Expo.(APEC)*, Mar. 2014, pp. 2746-2753.

[33] M. Jaksicet Z. Shen, I. Cvetkovic, D. Boroyevich, R. Burgos and P. Mattavelli,, “Nonlinear sideband effects in small-signal input dq admittance of six-pulse diode rectifiers,” in *Proc. Appl. Power Electron. Conf. Expo.(APEC)*, Mar. 2013, pp. 2761-2768.

[34] A. Riccobono, M. Mirz, and A. Monti, “Noninvasive online parametric identification of three-phase AC power impedances to assess the stability of grid-tied power electronic inverters in LV networks,” *IEEE J. Emerg. Sel. Top. Power Electron.*, vol. 6, no. 2, pp. 629-647, June. 2018.

[35] J.Huang, “AC/DC power system small-signal impedance measurement for stability analysis,” Ph.D dissertation, Dept. Elect. Eng., Missouri University of Science and Technology, Missouri, USA, 2009.

[36] J. Jokipii, T. Messo and T. Suntio, “Simple method for measuring output impedance of a three-phase inverter in dq-domain, in *Proc Power Electronics Conference (ECCE ASIA)*, Hiroshima, 2014, pp. 1466-1470.

[37] G. Francis, “An algorithm and system for measuring impedance in DQ coordinates,” Ph.D. dissertation, Dept. Elect. Eng., Virginia Tech, Blacksburg, USA, 2010.

[38] M. Cespedes and J. Sun, “Adaptive control of grid-connected inverters based on online grid impedance measurements,” *IEEE Trans. on Sustainable Energy*, vol. 5, no. 2, pp. 516-523, April. 2014.

[39] Z. Shen, M.Jaksic, B.Zhou, P.Mattavelli, J.Verhulst, M.Belkhayat, “Analysis of Phase Locked Loop (PLL) influence on DQ impedance measurement in three-phase AC systems,” in *Proc. Appl. Power Electron. Conf. Expo*., Mar. 2013, pp. 939–945.

[40] P. Guillaume, R. Pintelon and J. Schoukens, “Parametric identification of two-port models in the frequency domain,” in *Proc Conference Record. IEEE Instrumentation and Measurement Technology Conference*, Atlanta, GA, USA, 1991, pp. 263-271.

[41] L. He and C. Liu, “Parameter identification with PMUs for instability detection in power systems with HVDC integrated offshore wind energy,” *IEEE Trans. Power Systems*, vol. 29, no. 2, pp. 775-784, March 2014,

[42] S. Neshvad, S. Chatzinotas and J. Sachau, "Wideband identification of power network parameters using pseudo-random binary sequences on power inverters", *IEEE Trans. Smart Grid*, vol. 6, no. 5, pp. 2293- 2301, Sept. 2015

[43] B. Miao, R. Zane, and D. Maksimovic, "System identification of power converters with digital control through cross-correlation methods," *IEEE Trans. Power Electron*., vol. 20, no. 5, pp. 1093–1099, Sep. 2005.

[44] B. Wen, D. Boroyevich, P. Mattavelli, Z. Shen and R. Burgos, "Experimental verification of the Generalized Nyquist stability criterion for balanced three-phase ac systems in the presence of constant power loads," in *Proc 2012 IEEE Energy Conversion Congress and Exposition (ECCE)*, Raleigh, NC, 2012, pp. 3926-3933.

[45] Z. Shen. "Online measurement of three-phase AC power system impedance in synchronous coordinates" Ph.D. dissertation, Dept. Elect. Eng., Virginia Tech, Blacksburg, USA, 2012.

[46] V. Valdivia, A. Lázaro, A. Barrado, P. Zumel, C. Fernández and M. Sanz, "Impedance identification procedure of three-phase balanced voltage source inverters based on transient response measurements," *IEEE Trans. Power Electron.*, vol. 26, no. 12, pp. 3810-3816, Dec. 2011.

[47] A. Riccobono, E. Liegmann, M. Pau, F. Ponci and A. Monti, "Online parametric identification of power impedances to improve stability and accuracy of power hardware-in-the-loop simulations," *IEEE Trans. Instrumentation Measurement*, vol. 66, no. 9, pp. 2247-2257, Sept. 2017.

[48] A. Rygg and M. Molinas, "Apparent impedance analysis: A small-signal method for stability analysis of power electronic-based systems," *IEEE J. Emerg. Sel. Top. Power Electron.*, vol. 5, no. 4, pp. 1474-1486, Dec. 2017

[49] M. Jaksic *et al.*, "Medium-voltage impedance measurement unit for assessing the system stability of electric ships," in *Proc 2018 IEEE Power & Energy Society General Meeting (PESGM)*, Portland, OR, 2018, pp. 1-1.

[50] B. Wen, D. Boroyevich, R. Burgos, P. Mattavelli and Z. Shen, "Small-signal stability analysis of three-phase AC systems in the presence of constant power loads based on measured d-q frame impedances, *IEEE Trans. Power Electron*. vol., vol. 30, no. 10, pp. 5952-5963, Oct. 2015.

[51] V. Valdivia, P. Mattavelli, B. Wen, M. Jaksic, A. Lazaro and A. Barrado, "Confidence analysis on identification results of three-phase voltage source

inverters d-q impedance from transient response to load steps," in *Proc. Appl. Power Electron. Conf. Expo.*, March 2013, pp. 2726-2733.

[52] T. Roinila, J. Huusari and M. Vilkko, "On frequency-response measurements of power-electronic systems applying MIMO identification techniques," *IEEE Trans. Ind. Electron.*, vol. 60, no. 11, pp. 5270-5276, Nov. 2013.

[53] R. Luhtala, T. Roinila and T. Messo, "Implementation of real-time impedance-based stability assessment of grid-connected systems using MIMO-identification techniques," *IEEE Trans. Ind. Appl.*, vol. 54, no. 5, pp. 5054-5063, Sept. 2018.

[54] T. Roinila, T. Messo and E. Santi, "MIMO-identification techniques for rapid impedance-based stability assessment of three-phase systems in DQ domain," *IEEE Trans. Power Electron.*, vol. 33, no. 5, pp. 4015-4022, May 2018.

[55] T. Roinila, T. Messo and A. Aapro, "Impedance measurement of three phase systems in DQ-domain: Applying MIMO-identification techniques," in *Proc. Energy Convers. Congr. Expo*. Sep. 2016, pp. 1-6.

[56] I. Cvetkovic, M. Jaksic, D. Boroyevic, P.Mattavelli. F. C. Lee, "Un-terminated, low-frequency terminal-behavioral d-q model of three-phase converters," in *Proc. Energy Convers. Congr. Expo*. Sep. 2011, pp. 791-798.

[57] T. Roinila, H. Abdollahi, S. Arrua and E. Santi, "Real-time stability analysis and control of multi-converter systems by using MIMO-identification techniques," *IEEE Trans. Power Electron.*, vol. 34, no. 4, pp. 3948-3957, April 2019.

[58] V. Valdivia, A. Lazaro, A. Barrado, P. Zumel, C. Fernandez and M. Sanz, "Black-box modeling of three-phase voltage source inverters for system-level analysis," *IEEE Trans. Ind. Electron.*, vol. 59, no. 9, pp. 3648-3662, Sept. 2012.

[59] V. Valdivia, A. Barrado, A. LÁzaro, P. Zumel, C. Raga and C. FernÁndez, "Simple modeling and identification procedures for "black-box" behavioral modeling of power converters based on transient response analysis," *IEEE Trans. Power Electron.*, vol. 24, no. 12, pp. 2776-2790, Dec. 2009.

[60] V. Valdivia, A. Lázaro, A. Barrado, P. Zumel, C. Fernández and M. Sanz, "Black-box modeling of three phase voltage source inverters based on transient response analysis," in *IEEE Applied Power Electronics Conference and Exposition (APEC)*, Palm Springs, CA, 2010, pp. 1279-1286

[61] G. Guarderas, A. Francés, R. Asensi and J. Uceda, "Large-signal black-box behavioral modeling of grid-supporting power converters in AC microgrids," in

Proc. IEEE Appl. Power Electron. Conf. (APEC 2017), San Diego, CA, 2017, pp. 153-158.

[62] L. Ljung, *System Identification: Theory for the User, 2nd Edition*. Englewood Cliffs, Nj: Prentice-Hall, 1999.

[63] I. Rolf; M. Marco. "*Identification of Dynamic Systems: An Introduction with Applications*. New York, NY, USA: Springer, 2011.

[64] M. Zhang, X. Wang, D. Yang and M. Christensen, "Artificial neural network based identification of multi-operating-point impedance model," *IEEE Trans. Power Electron.*, early access, 2020.

[65] W. Liu, X. Xie, J. Shair and X. Li, "A nearly decoupled admittance model for grid-tied VSCs under variable operating conditions," *IEEE Trans. Power Electron.*, vol. 35, no. 9, pp. 9380-9389, Sept. 2020.

[66] D. Kincaid and W. Cheney, *Numerical Analysis*, 3rd ed. Providence, RI, USA: American Mathematical Society, 2009, pp. 478–492

[67] H. W. Reddick and F. H. Miller, *Advanced Mathematics for Engineers*, 3rd ed. New York, NY, USA: Wiley, 1955.

[68] X. Yue, Z. Fang, F. Wang, Z. Zhang and H. Shi, "A novel adaptive frequency injection method for power electronic system admittance measurement," *IEEE Trans. Power Electron.*, vol. 29, no. 12, pp. 6700-6711, Dec. 2014.

Appended Publications

ISSN (online): 2446-1636
ISBN (online): 978-87-7210-864-3 AALBORG UNIVERSITY PRESS